Evaporation Characteristics of a Liquid Bio-Fuel from Chicken Litter

Erik Tolonen

Thesis submitted to the Faculty of Graduate and Postdoctoral Studies in partial fulfillment of the requirements for the Master of Applied Science degree in Mechanical Engineering

Ottawa-Carleton Institute for Mechanical and Aerospace Engineering
Department of Mechanical Engineering Faculty of Engineering University of Ottawa

Abstract

Alternative fuels are becoming more important as fossil fuels become more expensive. This thesis describes the production and properties of a bio-oil produced from waste biomass, in this case chicken litter. A higher quality fuel was produced through thermal and chemical upgrading of the raw bio-oil; this fuel is similar in some respects to fossil fuels, as it has a high hydrocarbon content and energy density comparable to gasoline.

Combustion of liquid fuels commonly occurs in clouds of droplets, and studying the evaporation of single liquid drops provides information on the evaporation characteristics of the fuel as a whole. Droplet evaporation tests on the chicken litter fuel were carried out using the suspended droplet/moving furnace technique. For some tests, a fine wire thermocouple was used as the droplet suspension in order to measure the distillation characteristics of the fuel. An existing computational model based on continuous thermodynamics was used to model the evaporation of the fuel. The modelled composition of the fuel was based on an existing pyrolysis field ionization mass spectrometry (Py-FIMS) analysis and used five major groups of compounds. The properties for these groups required for the model were determined using several prediction methods and the values then used in a numerical model.

Model predictions of droplet temperatures calculated for the fuel showed good agreement with the measured temperatures, indicating that the modelled composition gave an accurate picture of the fuel. Droplet evaporation histories also agreed well with measurements, but were not capable of reproducing the observed disruption of the droplet produced by internal boiling at higher temperatures, nor the formation of a solid residue at the end of evaporation. Further enhancements to the model should allow the prediction of residue formation.

Sommaire

Cette thèse décrit la production et les propriétés d'un carburant liquide produit des fumiers de poulet. L'huile biologique crue était raffinée par des processus chimiques et thermiques pour produire un carburant liquide qui contient beaucoup d'hydrocarbures, comme les carburants pétrolières.

La combustion des carburants liquides commence avec l'évaporation des gouttelettes. On a fait des expériences sur l'évaporation de ce carburant comme gouttelettes seules, en utilisant la méthode de la gouttelette suspendue d'une fibre de quartz avec un four mouvant. Pour quelques expériences, on a utilisé un thermocouple de fil mince pour suspendre la gouttelette, à fin de mésurer le comportement de distillation du carburant. Un modèle numérique déjà existant, qui utilise les principes de la thermodynamique continue pour représenter la composition du carburant, était appliqué pour calculer l'évaporation des gouttelettes. La composition du carburant pour le modèle numérique était basée sur un analyse PyFIMS (pyrolysis field ionization mass spectrometry), qui a identifié cinq groupes principaux de composants chimiques. Les propriétés thermiques pour ces groupes chimiques pour le modèle numérique sont déterminées par divers méthodes pour l'évaluation des propriétés.

Les températures de la gouttelette prédites par le modéle numérique sont en bon accord avec les expériences, ce qui indique que la composition du carburant est bien représentée par le modéle. Le progrés du diamétre de la gouttelette avec le temps était aussi bein prédit, mais le modèle est incapable de calculer deux phénomènes, ni l'ébullition intérieure de la gouttelette à hautes températures ni la formation d'un résidu solide à la fin de l'évaporation.

Acknowledgements

The author gratefully acknowledges the financial the support of NSERC which provided funding for this project.

The author also wishes to acknowledge Dr. Carlos Monreal and Dr. Morris Schnitzer of the Dept. of Agriculture who provided many of the resources used in this project. Without their support none of this would have been possible. Thanks are also due to Dr. Peter Fransham of ABRITech for providing equipment and samples as well as introducing me to the area of bio-fuels and bio-energy. I would also like to thank my girlfriend, Kristen Hearns, for her support during the writing of this thesis.

A special thanks goes to Dr. Hallett for his guidance and support throughout the duration of this project. His expertise and assistance were essential to its success and the further study of bio-fuels. It was a honour and privilege to be his student.

Nomenclature

m/z: Mass to charge ratio

h: Height (mm)

w: Weight (mm)

V: Volume (mm^3)

π: Pi: (3.14159)

d: Droplet Diameter (mm)

Q: Heat Conduction (W/m^2)

λ: Thermal Conductivity (W/mK)

A: Area (m^2)

T_∞: Surrounding Temperature (K)

T_R: Droplet Temperature (K)

δ: Boundary Layer Thickness

α: Shape Parameter

β: Inverse Scale Parameter

$\Gamma(\alpha)$: Gamma Function

σ: Standard Deviation

θ: Distribution Mean

T_B: Boiling Temperature (K)

N_K: Number of Groups

$tb1k$: Boiling Point Group Weight

T_{cr}: Critical Temperature

$tc1k$: Critical Temperature Group Weight

P_{cr}: Group weighting factor for critical pressure

$pc1k$: Critical Pressure Group Weight

M_i: Molecular weight of species i

h_{fgi}: Enthalpy of vaporization

hvk: Enthalpy of vaporization group weight

Φ_H: Watson relation for temperature correction

C_{pL}: Liquid Specific Heat

a_i,b_i,d_i: Group weights for liquid specific heat

C_{P^o}: Vapour specific heat

C_pA_k, C_pB_k, C_pC_k, C_pD_k: Group weights for vapour specific heat

D_{AB}: Diffusion coefficient (m^2/s)

P: Pressure (Bar)

M_{AB}: Reduced molecular mass

ϵ_{AB}: Lennard-Jones interaction energy

σ_{AB}: Lennard-Jones interaction length

Ω_D: Collision integral

T^*: Non-dimensional temperature

k: Boltzmann's constant

Φ_D: Temperature dependence for diffusion correlation

b_Φ: Optimization for temperature dependance term

λ: Thermal conductivity (W/mK)

$M^{'}$: Molecular Weight (g/mol)

C_v: Constant volume heat capacity (J/kmol)

R: Gas constant (8.314)

η: Viscosity (Pa s)

V_C: Critical Volume (m^3)

ν: Specific Volume (cm^3/mol)

Contents

List of Tables

List of Figures

1 Introduction

The evaporation behaviour of fuels is of great importance to combustion researchers, since liquid fuels must be evaporated and burn as a vapour. This thesis examines the evaporation behaviour of a liquid fuel produced by upgrading a bio-oil produced by the pyrolysis of raw chicken litter, a fuel which in some ways looks similar to a refined fossil fuel.

A method which is widely used for droplet evaporation testing is the suspended droplet/moving furnace technique, in which a small droplet is suspended on a quartz fibre before being exposed to a furnace in which it is rapidly heated. The whole process is monitored, allowing the changes in the drop size to be determined as a function of time. These results, together with those from parallel computational modelling, allow one to draw conclusions on how these fuels can be successfully used in many processes such as internal combustion engines or heating systems.

1.1 Fuels from Biomass

Many fuels today have a renewable component, sometimes as required by government mandates. This is encouraging companies to focus on the development of environmentally friendly and sustainable green fuels. Fossil fuel supplies are expected to decrease in coming decades, and although technologies for reaching previously unreachable fossil fuel sources exist, the risks and expenses of extracting them are greater.

Biomass presents an interesting opportunity for the production of liquid fuels from low energy source biomass waste. Much of this waste would otherwise be disposed of in landfills where it would add to the current problems of landfilling. The thermochemical conversion of biomass, particularly agriculture wastes, into liquid fuels is currently being researched at Agriculture Canada. It is believed to have a strong potential for reducing the amount of waste that is landfilled, as well as providing new sources of fuels and energy.

One of the methods for producing liquid fuels is the process of fast pyrolysis which

involves the rapid heating of biomass to temperatures above 300°C using a stirred bed and the rapid cooling of the vapours produced. When condensed these vapours form a thick dark viscous liquid called biomass pyrolysis oil or bio-oil. It somewhat resembles crude oil, but is quite different in properties. Bio-oil can be separated into different components and useful compounds can be extracted, providing chemicals for industry, medical and other areas as well as fuel precursors which can be upgraded to produce automotive grade fuels.

Bio-oil is commonly produced from wood and waste wood products such as sawdust. It can however be produced from a wide variety of wastes. In the literature many sources have been identified and each of the bio-oils produced will have its own unique composition. The overall properties of most bio-oils will however be similar.

The fuels studied here were produced from raw chicken litter, a mixture of poultry manure and bedding. When dried this was light brown in colour and easily crumbled into small particles with a slight unpleasant odour; easier for the operator to tolerate than the moist material collected from the farm. Through a series of physical and chemical steps the litter was converted into bio-oil and the bio-oil refined into a higher quality fuel.

1.2 Droplet Evaporation Theory

The combustion of liquid fuels requires them first to be vaporized before combustion can take place. A common method is the atomization of the fuel into droplets which burn together in a cloud. In order to understand the overall spray behaviour one first needs to understand the evaporation of a single droplet (Law, 2006).

The simplest model for droplet evaporation theory is the d^2 law of droplet vaporization. A single spherical droplet consisting of a pure compound at ambient temperature is immersed in a hot environment at T_∞. Heat from the surroundings is conducted into the droplet, increasing its temperature. As the temperature of the droplet increases, the vapour flux of fuel from the droplet to the surroundings increases. Since the rate of change of the gas phase processes is much greater than those occurring at the droplet

surface, we can therefore consider the vapour phase to remain constant. This is called the quasi-steady state approximation (Hallett 2000; Law 2006).

The temperature of the droplet will increase and approach the boiling temperature but the droplet will evaporate without reaching it and the maximum temperature obtained is called the equilibrium vaporization temperature. This is the temperature at which the heat and mass fluxes are in equilibrium.

Initially the droplet will expand due to an increasing specific volume as its temperature increases. As mass diffuses from the droplet it will begin to shrink. The rate at which the droplet shrinks usually approximately follows a relationship in which the diameter squared (d^2), decreases linearly with time (Law, 2006).

1.3 Scope of Research

We have set out to determine the evaporation characteristics of a liquid fuel produced by the process of fast pyrolysis of chicken litter, and refined through subsequent physical and chemical upgrading. A computational model previously developed (Hallett, 2000; Tamim and Hallett, 1995) will be used to model the fuels behaviour under evaporative conditions. The goal of this research is to investigate the evaporation characteristics of this fuel using droplet evaporation testing and compare the results to a numerical model which uses the technique of continuous thermodynamics to model the mixture composition. The numerical model used here was previously developed to model evaporation of fuels containing many components such as diesel or gasoline. It has successfully been used to model a variety of fuels including bio-fuels such as biodiesel. It has also been used to model bio-oil produced from the pyrolysis of wood (Hallett and Clark, 2006).

A literature survey was first conducted to examine the information available on the topics of production and upgrading of bio-oils, their combustion and evaporation behaviour, continuous thermodynamics and fuel droplet modelling. The details of the production and upgrading of the bio-oil are then discussed. Several different physical and chemical processes were used to produce the fuel; the reasoning for these is explained

and results presented. The experimental section describes the temperature and droplet evaporation tests which were performed, the apparatus used and data analysis procedure. The computational model used to make predictions for the fuel behaviour is then presented. Finally, the experimental results are presented and compared to the predictions of the numerical model.

2 Survey of Literature

A literature survey was performed to outline work which has been done on the production of bio-oil from biomass and agricultures wastes, on droplet combustion and evaporation behavior of these fuels, and on the techniques of continuous thermodynamics as applied to modeling droplet evaporation. The research conducted in this thesis builds upon these topics.

2.1 Liquid Fuels from Biomass

The production of liquid fuels from biomass has been studied for some time and has recently gained renewed interest, mainly due to the rise in prices of fossil fuels, but also as a method for the disposal of waste biomass and production of bio-products. The conversion of biomass to liquid fuels is expected to provide new economic opportunities as well as improving the sustainability of rural communities (Schnitzer et al., 2007a).

The management of animal manure presents challenges in many areas of agriculture. With an increasing amount of livestock comes an increase in the amount of manure requiring safe disposal. Recent changes to government regulations have tightened the requirements for land applications, such as the spreading of manure as fertilizer. Therefore it is beneficial to seek more sustainable methods for its management and disposal (Schnitzer et al., 2007a).

Modern poultry production occurs on large industrial scale farms containing upwards of 25,000 birds, thus producing large amounts of manure. Traditionally this manure was disposed of by spreading it on the land as a fertilizer to meet the nitrogen requirements of the soil; this however can result in an excess of phosphorus which can be transported into lakes and streams through runoff (Whitely et al., 2006).

Combustion has been proposed as a possible disposal method. According to Whitely et al. (2006) chicken manure has a high energy content, approximately 12,000 kJ/kg. This paper has cited studies which have proposed the combustion of the manure for the

generation of energy and heat to supply the farms.

2.1.1 Production and Properties of Bio-Oil

Pyrolysis can be used to thermo-chemically convert waste into bio-fuels and bio-products. It is seen as a sustainable method for the disposal of waste but also for the production of value-added products (Schnitzer et al., 2007a). Bio-oil, or as it is sometimes called, bio-crude, is a thick black liquid which resembles the crude oil from which fossil fuels are derived. Like fossil fuels bio-oil contains numerous compounds; however, compared to fossil fuels the types of chemical compounds represented are very different.

Schnitzer et al. (2007a) have studied liquid fuels produced by the flash pyrolysis of chicken litter. Flash pyrolysis involves the rapid heating of biomass and quenching of the vapours produced. The type of reactor used mixed the biomass with stainless steel shot at a temperature of approximately 330°C and a residence time of 1 to 2 seconds. The oil produced was observed to separate into two layers after sitting for approximately 6 hours. The top light aqueous layer was termed fraction I and the bottom heavy layer fraction II. High levels of oxygen were detected in the oil, 37.6 % by mass in fraction I and 14.3 % by mass in fraction II (Schnitzer et al., 2007a,b).

Research performed at Agriculture Canada by Schnitzer et al. (2007a,b) has focused on the separation and analysis of bio-oil fractions produced by the pyrolysis of chicken litter. This work has been successful in identifying a considerable amount of compounds present in the raw chicken manure and bio-oil fractions, which have been grouped into the following categories: i) heterocyclic nitrogen compounds, ii) substituted furans, iii) phenol and substituted phenols, iv) benzene and substituted benzenes, v) carbon-containing ring structures and vi) aliphatics.

Schnitzer et al. (2007a,b) provide a listing of many individual compounds which were identified in the bio-oil, including n-alkanes and 1-alkenes containing chain lengths of 7 carbons or greater, as well as many aromatic compounds. Detection was accomplished by the processes of pyrolysis field ionization mass spectrometry (Py-FIMS) and gas chro-

matography with mass spectrometry (GC-MS) among others. The analysis of the bio-oil fractions showed a variety of compounds including a considerable amount of aliphatics ranging from C_7 to C_{17}.

Kazi et al. (2011) analyzed individual fractions separated from the oil analyzed by Schnitzer et al. (2007a). In these fractions over 500 chemical compounds were detected, most of them containing nitrogen. Two distinct groups were recovered, a clear group containing mostly hydrocarbons, with some steroids and sterols present, and a nitrogen group containing primarily nitrogen compounds.

There is little other literature available on the specific topic of bio-oils based on chicken waste. However, bio-oils produced by pyrolysis of wood and other solid biomass are similar in many respects, and therefore will be included in this literature survey.

Many researchers have studied the properties of bio-oil from wood and other agricultural materials. Oasmaa and Czernik (1999) have studied in detail bio-oils produced from wood pyrolysis. Their use as fuels in conventional engines and combustors is still limited owing to the oils' unfavorable properties. One of the drawbacks is the heating value: the gross heating value for the heavy fraction produced from chicken litter was determined to be 27.9 MJ/kg (Schnitzer et al., 2007a). The lower heating values for oils produced from various types of wood range from 13 to 18 MJ/kg (Oasmaa and Czernik, 1999). For comparison, fossil fuels are much higher ($\sim$46 MJ/kg for conventional gasoline). This difference is mainly due to high levels of oxygen present in the bio-oils. Other unfavorable factors are high viscosity, acidity and the polymerization of compounds over time, resulting in the oil becoming more viscous with age (Oasmaa and Czernik, 1999).

(Yanik et al., 2007) has studied the composition of bio-oils from flash pyrolysis of agricultural wastes and analyzed the composition using gas chromatography-mass spectrometry (GC-MS). Their results showed that the oil contained water, carboxylic acids, carbohydrates and lignin-derived substances. Two phases were observed to form, a water-soluble phase and a hexane-soluble phase; this was consistent with the observations of Schnitzer et al. (2007a,b) for chicken litter oil. The water-soluble phase was found to

contain volatile acids, alcohols and sugars; the water-insoluble phase, lignin-derived materials. The largest contribution was from acetic acid and non-aromatic ketones; also detected were hydroxypropanone, butanone derivates and saturated and unsaturated five membered cyclic ketones (Yanik et al., 2007).

Scholze and Meier (2001) studied the properties of wood bio-oil using gas chromatography and some of their findings were similar to those of Oasmaa and Czernik (1999). A large number of oxygenated compounds was detected and tests confirmed the presence of methoxyl (R-O-CH_3) and hydroxyl (R-OH) functional groups. The use of Fourier transform infrared spectrometry (FTIR) also showed the presence of oxygen in carbonyl groups (A-(C=O)-B).

In a study by Pokorna et al. (2009) bio-oil produced from sewage sludge was studied and found to also contain oxygenated hydrocarbons, carboxylic acids, fatty acids and alcohols among other compounds. Small amounts of steroids such as cholestene, cholestadiene and cholestanol were also detected. The presence of sterols was detected in bio-oil produced from chicken manure as determined by Kazi et al. (2011).

2.1.2 Separation and Upgrading

The presence of oxygen in bio-oil was shown to contribute to a variety of issues which makes its use as a fuel difficult. Bio-oil has a tendency to polymerize over time, thus increasing its viscosity. The presence of oxygen also contributes to a lower energy content. The removal of oxygen is expected to solve some of these problems. Maggi and Delmon (1994) have proposed the upgrading of wood bio-oils by deoxygenation and hydrotreating with some success. This is expected to increase the heating value due to the elimination of oxygen; this can also reduce polymerization attributed to oxygen-containing groups. The amount of oxygen in bio-oil can be as high as 40 % by mass and exists in various chemical structures. These processes use specially prepared zeolite catalysts and moderate to high temperatures: hydrogenation from 100 to 200°C and hydrorefining from 350 to 425°C (Maggi and Delmon, 1994).

The compounds detected were separated into the following five categories: i) acids and phenols, ii) bases, iii) slightly polar compounds, iv) hydrocarbons and v) aqueous. Some of the parent compounds and their deoxygenated product compounds identified were: i) 4-methylacetophenone, transformed to ethylmethyl-benzene, ii) diethyldecanedioate to octane, nonane and decane, iii) 4-methylphenol to toluene and methyl-cyclohexane, iv) 2-ethylphenol to ethylbenzene and ethylcyclohexane, and v) dibenzofuran to biphenyl, bicyclohexane, cyclohexane and benzene (Maggi and Delmon, 1994).

In a study by Czernik and Bridgwater (2004) the upgrading of biooil from cellulose biomass was examined using two processes, hydrotreating and catalytic vapor cracking. Their results were similar to those of Maggi and Delmon (1994). Bio-oil was treated at high temperatures and with high pressure hydrogen, oxygen was rejected in the form of water, and the final product was similar to naphtha. Catalytic vapour cracking using zeolite catalysts was performed at 450°C and atmospheric pressure, oxygen was rejected in the form of water, CO_2 and CO. This produced mostly aromatics, possibly due to the low H/C ratio of the bio-oil. Processing costs were high and the final products were not fully compatible with fossil fuels (Czernik and Bridgwater, 2004).

Ott et al. (2008) analyzed the distillation curves produced from the distillation of a bio-crude which was produced by the batch pyrolysis of swine manure. Distillation was conducted by heating the bio-crude samples from ambient to approximately 300°C and collecting various fractions. The fractions were analyzed by gas chromatography with sulfur chemiluminescence detection (GC-SCD), a method for the analysis of sulphur compounds. The distillation fractions recovered showed a low and high boiling range: the low range (100 to 150°C) was found to contain mostly water, and the high range (300 to 500°C) to contain long-chain hydrocarbons. Also detected in the high boiling range were sterols, alkylbenzenes, indanes, tetralins and naphthalenes. The majority of sulphur detected was in the fractions between 120 and 373°C.

Kazi et al. (2011) worked on the separation and identification of heterocyclic nitrogen compounds at Agriculture Canada. Upgrading of raw viscous bio-oil from chicken

litter (termed heavy bio-oil in previous studies (Schnitzer et al., 2007a,b)) was performed using microwave solvent extraction at a temperature of 120°C and pressure of 100 psi for 30 minutes. This upgraded bio-oil was fractionated into 15 individual samples by column chromatography and fractions 5 to 15 (nitrogen containing fractions) were used. Semi-quantitative analysis of the fractionated samples was performed using Py-FIMS; individual ion intensities for mass ranges from 15 to 900 Daltons were measured, the total ion intensity (TII) was then determined and the results normalized to a 1 μL sample. The base structures identified in the sample were: i) pyrazine, ii) benzo-quinoline, iii) carbazole, iv) phenylpyridine, v) indole, vi) pyrazole and vii) pyridine; many derivatives of these structures were also identified.

Garcia-Perez et al. (2007) developed a method for the characterization of compounds in wood bio-oil by a distribution parameter, either boiling point or molecular mass. Thermogravimetric analysis was used to characterize the sample by measuring the change in mass with temperature as components boiled off: this allowed different bio-oils to be quickly compared based on the mass curves produced. Tetrahydrofuran (THF) was used as a solvent to elute compounds based on their molecular mass. Their approach was to divide the compounds into macro chemical families based on their rate of elution. The compounds identified were grouped into the following classes: i) volatile non-polar, ii) volatile polar, iii) monolignols, iv) polar compounds with moderate volatility, v) sugars, vi) extractive-derived compounds, vii) heavy non-polar compounds, viii) heavy polar compounds.

The composition of bio-oil produced by the pyrolysis of waste biomass is significantly different from that of petroleum fuels. The number of individual compounds can be in the thousands, many of which exist in trace quantities. The raw bio-oil contains large amounts of oxygen in the form of oxygenated compounds which lowers the heating value of the oil. Upgraded fuels show a lower oxygen content and higher heating value with much of the carbon present in the form of aromatics (Czernik and Bridgwater, 2004).

2.1.3 Combustion and Evaporation Behaviour

Droplet evaporation of bio-oil from wood pyrolysis was previously studied by Hallett and Clark (2006) using the suspended droplet-moving furnace technique (droplet supported from a fibre support or a thermocouple). Quartz fibre experiments showed vigorous bubbling and disruptions in the droplet after the initial heating phase. Droplets were observed to swell and collapse multiple times a second; this behavior was attributed to the internal boiling of compounds with low boiling points inside the droplet.

Droplet combustion tests using a quartz supporting fibre were conducted at the Scandia National Laboratories. Droplets of various wood pyrolysis oils were suspended on quartz filaments and the square of the normalized droplet diameter $(d/d_o)^2$ plotted against residence time. Parallel experiments on No. 2 and No. 6 fuel oil were also plotted for comparison. The tests were conducted at 1600 K with an atmosphere of 24 mole-% O_2. The behavior of the bio-oils was found to be similar to that of No. 6 fuel oil. Both of the bio-oils studied showed evidence of microexplosions (droplet disruptions and internal boiling) (Shaddix and Hardesty, 1999).

To our knowledge there has been little research in the use of raw bio-oil as a primary fuel in an internal combustion engine. The numerous unfavorable properties of the oil (high viscosity, tendency to polymerize, formation of char residues in combustion) would likely result in poor operation or damage. There have however been studies in producing and using mixtures of fuels containing bio-oil with some success. Chiaramonti (2003) found that emulsions of bio-oil and petroleum diesel fuel could be used in a modified diesel engine. In their work various emulsifying agents were examined as well as to how they affected the properties of the fuel blends.

Shihadeh and Hochgrebl (2002) also examined the use of raw bio-oil as a fuel substitute in diesel engines. It was found that bio-oil has a longer ignition delay, which is likely due to small amounts of volatile compounds and poor spray characteristics. Ikura et al. (2003) tested different additives which they used to produce stable emulsions of bio-oil and diesel. A test of 30% bio-oil/diesel emulsion was successful in a diesel engine

without modifications. It was also found that emulsions, even with stabilizers could only be stored for a certain period of time before stratification would occur. Mixing would however reform the emulsion.

One of the difficulties in using pure bio-oil in diesel engines is that it has a low cetane rating, so that it is difficult to achieve autoignition without the use of additives (Czernik and Bridgwater, 2004). This was also reported by Ikura et al. (2003) who found that the addition of bio-oil to diesel lowered the cetane rating of the fuel. Czernik and Bridgwater (2004) showed that a blend of 24% methanol, 72% bio-oil with the addition of 4% tetraethyleneglycol dinitrate could improve the cetane rating and achieve results similar to that of petroleum diesel.

Research into the combustion of bio-oil in gas turbines was performed by Juste and Monfort (2000) who compared the results of bio-oil with those of standard petroleum fuels. In the case of bio-oil, small modifications were necessary to the injection and ignition system. Additional tests were performed using bio-oil-ethanol blends (80%-20%) with performance similar to standard fuels. It was however noted that there was a decrease in the operational range of the turbine during the use of bio-oil and bio-oil blends.

Zhang and Kong (2012) developed a multicomponent droplet evaporation model which they used for modeling bio-oil and bio-oil fuel mixtures. Their analysis of wood bio-oil identified 40 major compounds which they put into the following categories: i) carbohydates, ii) furans, iii) phenols, iv) guaiacols, v) syringols and vi) water. Their modeling of the fuel used a discrete approach in which individual compounds were chosen from each category, and groups with low concentration were modeled using a single component. Overall ten compounds with significant mass fractions were selected, and their values were increased to compensate for those which were not considered. The evaporation of bio-oil was studied as well as blends of bio-oil with diesel, bio-oil with bio-diesel and bio-oil with ethanol.

Zhang and Kong (2012) also conducted evaporation studies using the KIVA-3 V nu-

merical model and the simulated conditions chosen were for those of an internal combustion engine cylinder. Tests were performed using bio-oil and blends of bio-oil with diesel and ethanol. The results found that the fuel blends produced droplet lifetimes which were greater than that of pure bio-oil and pure No. 2 diesel: the blended fuel droplet lifetimes were found to be three times that of diesel and four times that of ethanol.

2.2 Continuous Thermodynamics

The technique of continuous thermodynamics provides a framework for modeling systems which contain a large number of compounds. It uses one or more probability density distributions to describe the mixture instead of listing all of the compounds present in it. The type of distribution function chosen should be that which best approximates the system; in the literature a gamma distribution is commonly used. It is important to note however that this approach is valid only with mixtures containing a large number of compounds, since only with many components can the mixture composition be approximated as varying continuously with the distribution variable.

The probability $f(x)$ of a distributed variable x is determined by distribution function parameters: the mean θ, standard deviation σ and sometimes higher moments as well. For a fuel the distributed variable commonly used is the molecular weight; equations for the values of thermodynamic parameters can then be derived in terms of the molecular weight.

The method has been used in chemical process design for modeling the distillation of petroleum and the results of polymerization reactions, among other applications. Chou and Prausnitz (1986) presented one such framework which they used to perform flash calculations of a commercial petroleum fuel. They compared their results with models of the same system using pseudocomponents and found that the selection of compounds chosen was important, as different choices would provide different results.

Using a similar method, Cotterman and Prausnltz (1985) compared pseudocomponent methods with continuous and semi-continuous methods, and used these to calculate the

bubble and dew points for a mixture containing CO_2 and paraffins. Their results showed good agreement for the bubble point which they reported wasnt as sensitive to the chosen method. The dew point however showed considerable deviations depending on the method used to characterize the mixture. The reported reason for this was the way the heavy compounds were characterized.

Willman and Teja (1986) used continuous thermodynamics to predict the dew points of natural gas condensates, absorber oils, aromatic light oils, coal liquids and crude oil. The results of these were compared with a discrete components model. It was found that the predictions of the continuous model showed a much better agreement with experimental results then did the results of the discrete model.

2.2.1 Fuel Droplet Modeling

Tamim and Hallett (1995) first applied the method of continuous thermodynamics to predict the evaporation behavior of fuel droplets. They found that this method provided a realistic representation of the observed evaporation and combustion behavior for multicomponent fuels. Previous studies considered mixtures of only discrete components, mostly binary mixtures. To accurately model the mixture one needs a method to model the entire composition. In a mixture containing components with widely varying boiling points, transport processes can affect the surface composition and therefore the evaporation. Hallett (2000) presented a simplified continuous thermodynamics model which is easier to use than the full model used by Hallett and Tamim described above. This provided a simple quasi-steady state solution which could be applied to two limiting cases, the well-mixed and diffusion-limiting case. It can also be incorporated into a full spray combustion model.

A study by Lippert and Reitz (1997) applied the continuous thermodynamics of Tamim and Hallett (1995) to model the multidimensional evaporation of droplets in a spray in a Diesel engine cylinder and compared these results with those computed using a pseudocomponent model.

Ra and Reitz (2003) developed a complex multi-component three dimensional model using continuous thermodynamics, which was used to model the evaporation of gasoline in a direct injection (GDI) engine. Of particular interest to them was evaporation under low temperatures and low pressure.

Clercq and Bellan (2005) modeled the three-dimensional evaporation of multi-component fuels in sprays using probability distribution functions (PDFs). They then compared this model to one using discrete component fuels and found substantial differences between the global and local mixing features of the layers. Their conclusions were that single component fuels were unable to capture the necessary species distribution for a complete model of combustion. Several studies investigated the computational use of a model combining discrete components and continuous methods, a combination often referred to as semi-continuous. The discrete compound method was found to require a greater computational overhead for a large amount of compounds (Ra and Reitz, 2003).

2.2.2 Applications to Bio-oils

Modeling droplet evaporation of fuels such as bio-oil was accomplished using the process of continuous thermodynamics, as proposed by Tamim and Hallett (1995). A continuous thermodynamics model was developed to describe the vaporization of droplets of multi-component fuels. Transport equations were derived for the distribution function which describes the mixture composition, and relations for properties were developed Tamim and Hallett (1995).

Hallett and Clark (2006) applied this model described above to droplets of wood pyrolysis oil using several distribution functions for the main chemical families present. The model was observed to give reasonable results in predicting the major events in the lifetime of the droplet: initial heating, evaporation of volatiles and pyrolysis of non-volatile compounds. Since detailed composition information for these fuels is difficult to obtain, trials were performed in which the composition was varied to determine its effect on the droplet evaporation. In the case of volatiles there was no significant deviation;

however, additional water was found to slow the progress of evaporation due to its high enthalpy of vaporization.

These studies have shown that the method of continuous thermodynamics provides accurate predictions and achieves results which closely predict those from experimentation. Modeling of complex fuels such as bio-oil is also possible even if complete composition information is unavailable.

3 Production and Composition of Upgraded Bio-oil

The fuel which was studied herein was produced through a variety of physical and chemical processes which converted the raw material into the final product. It was then analyzed to determine its chemical makeup which is used for later computational modelling. The method used to produce and upgrade this fuel as well as the analysis are detailed below.

The conversion of raw chicken litter into bio-oil was performed at ABRITech Inc. by the author (Erik Tolonen) while under the supervision of Dr. Peter Fransham. All the equipment used to produce the bio-oil was manufactured by ABRITech Inc. The separation and upgrading of the raw bio-oil was also performed by the author at Agriculture Canada under the supervision of Dr. Carlos Monreal; this work had been accomplished prior to the starting of droplet evaporation research at The University of Ottawa. The pyrolysis field ionization mass spectrometry was performed by Dr. Gerald Jandl at the University of Rostock in Germany. The raw data was analysed at Agriculture Canada by Dr. Morris Schnitzer and Dr. Carlos Monreal, this analysis was used to develop the model composition explained in section 3.3.1.1.

Raw bio-oil was produced at ABRITech inc. at their facilities in North Gower, ON. using a bench scale reactor system shown in figure 3.1. The bio-oil was upgraded to produce a higher quality fuel at Agriculture Canada using microwave solvent extraction and column chromatography. Chemical analysis of the fuels composition was performed in Germany at the University of Rostock and the results reduced to a form suitable for numerical modelling at the University of Ottawa.

Raw chicken litter was obtained from a commercial chicken farm and dried until it reached a moisture content of approximately 10% as determined by weight. Water has a high enthalpy of vaporization and therefore it is advantageous to dry the biomass before conversion; this also improved its handling characteristics. The dried litter crumbled and easily formed a powder as it was crushed to reduce its particle size. This was then packed

into an auger tube and injected into a fixed bed reactor at a rate of approximately 1 gram/s. The temperature of the bed was maintained at approximately 375°C. The bed is composed of stainless steel shot with a diameter of approximately 3 mm and is agitated by a mechanical stirring device at a rate of approximately 30 rpm. This ensures a uniform bed temperature and mixes the biomass with the shot. Heat is supplied using an electric heater installed below the reaction chamber and the temperature is controlled using an Omega temperature controller connected to a thermocouple.

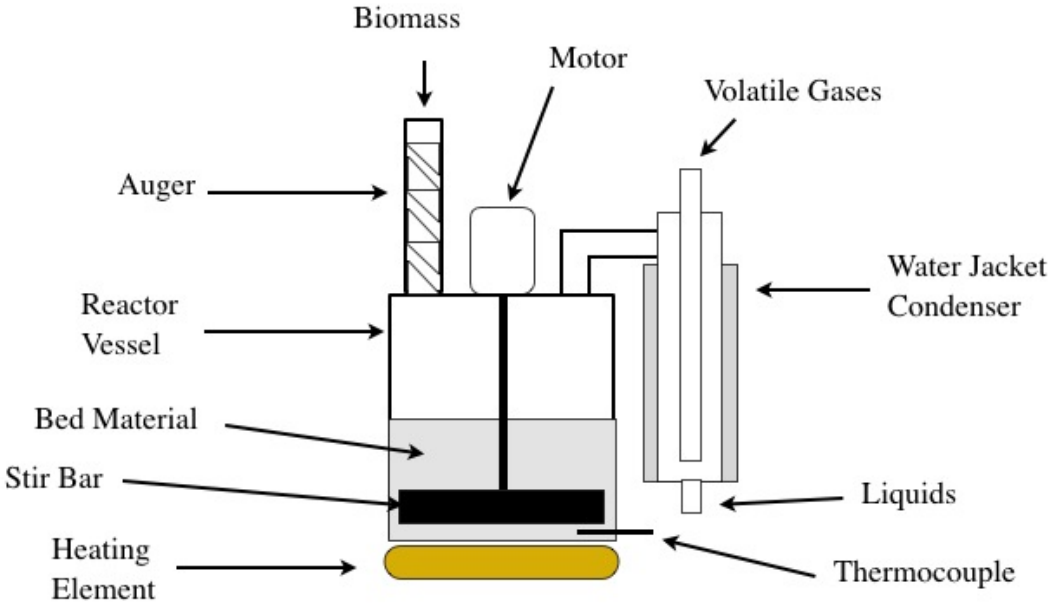

Figure 3.1: Bench Scale Pyrolysis Reactor

As the biomass mixed with the bed it was quickly converted to vapours and char. The char remained inside the reactor and the vapours exited through a port which connected it to the condenser. The vapours were condensed using a cold wall condenser which used water to keep the temperature at approximately 20°C. The condensed vapours were collected in sample jars by a valve located on the bottom of the condenser. Samples were taken to Agriculture Canada for separation and upgrading.

3.1 Receiving and Handling Procedures

Raw bio-oil was received from Advanced Bio-refinery Inc. (now ABRITech Inc.) in 1 L sample jars containing both heavy and light fractions mixed together. The bottom heavy fraction consisted of organic water-insoluble compounds which are of interest in this study, while the light fraction was an aqueous layer floating on top. Before any analysis was performed the aqueous layer was decanted by pouring it off. A small amount of water was soluble in the heavy organic fraction and could not be removed by this method. As the sample was allowed to sit small amounts of water were observed to come out of solution and float on the surface of the organic layer; these were decanted prior to use. Each time a sample was taken the jar was stirred using a stainless steel spatula to ensure the sample was uniformly mixed. Research has shown that bio-oil over periods of time shows signs of stratification (Garcia-Perez et al. 2007; Yanik et al. 2007). No additional stratification was observed to occur in the heavy fraction after the light fraction had been decanted.

3.2 Upgrading of Bio-oil

The raw bio-oil was upgraded using the techniques of microwave solvent extraction and column chromatography to remove any residual char and other unwanted compounds from the oil. This also acted to improve the chemical and physical characteristics and produce a fuel similar to fossil fuels.

Previous studies of the heavy bio-oil fraction conducted at Agriculture Canada showed large amounts of oxygen (14.4 % wt/wt) and nitrogen (7.4 % wt/wt) present in the sample as well as small amounts of char (0.4 % wt/wt) (Schnitzer et al., 2007a). The presence of oxygen will contribute to a lower heating value and it is therefore advantageous to remove it.

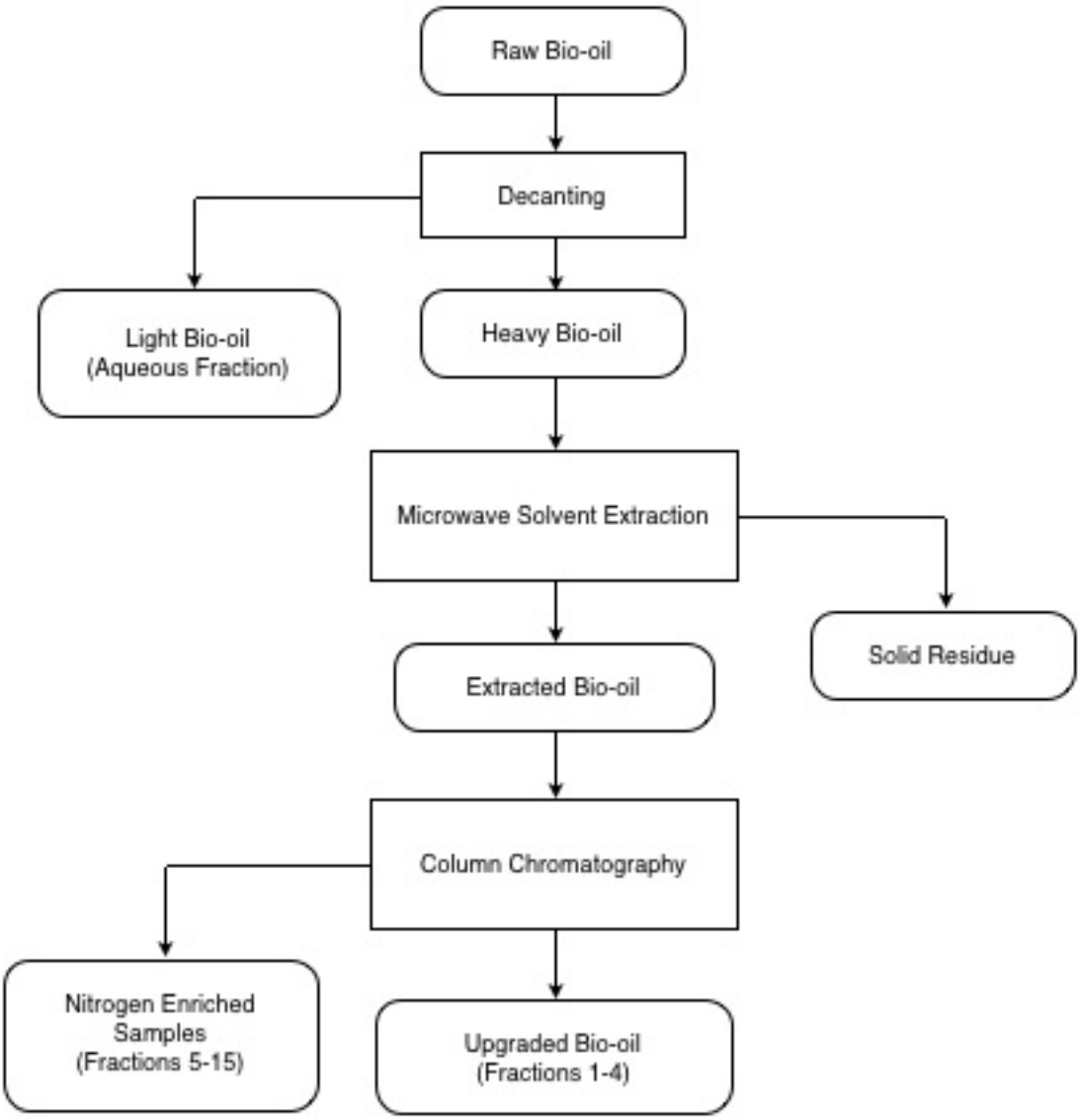

Figure 3.2: Bio-oil Upgrading Pathway

After the raw bio-oil has been decanted, leaving only the heavy fraction, an extracted bio-oil is produced by microwave solvent extraction of the raw bio-oil. The extracted bio-oil is next separated using column chromatography to produce an upgraded bio-oil which is the final product used for droplet evaporation studies.

3.2.1 Microwave Solvent Extraction

Solvent extraction is a commonly used chemical procedure in which material in a solid matrix is extracted into a liquid phase; this liquid phase can then be evaporated, leaving behind only the extracted compounds. A variation of this technique is microwave solvent extraction which makes use of the heat and pressure developed by a commercially available microwave system. The system contains a microwave cavity in which a sample vial containing the sample is placed. An infrared temperature sensor and a pressure sensor allow the real-time monitoring of the sample conditions. A magnetic stir bar placed in the vial allows the solvent to be agitated during heating and ensures a uniform solvent composition.

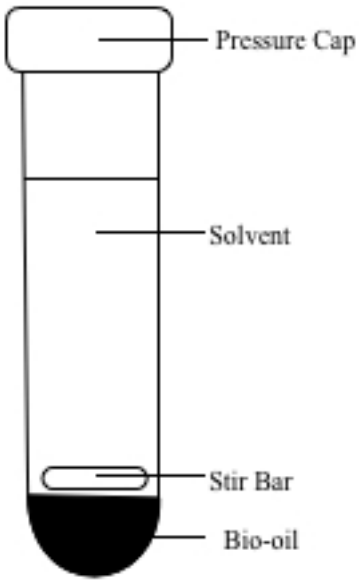

Figure 3.3: Microwave Pressure Vial

The purpose of microwave solvent extraction was to extract neutral compounds from the bio-oil, specifically hydrocarbons, therefore reducing the amount of oxygen and nitrogen containing compounds. This was expected to increase the energy content of the fuel and reduce many of the adverse properties of the heavy bio-oil (Monreal, 2009).

Previous work completed at Agriculture Canada was used to determine the optimum

conditions for the extraction of compounds from the heavy bio-oil. Microwave extraction consumes large amounts of energy and prolonged exposure to microwave radiation could have an effect on chemical reactions within the solid matrix. For these reasons it is beneficial to determine these conditions. Numerous trials were performed using various combinations of temperature, pressure and time. Extractions were performed at various temperatures from 50 to 300°C with times ranging from 5 to 30 minutes. The pressure developed is dependent on the type of solvent used and the temperature. The optimal conditions were determined to be 120°C and 20 minutes with a pressure reached of approximately 50 psi (Monreal, 2009).

To remove the oxygen a sample of the heavy fraction, which was separated above, was placed in an 80 mL reaction vial and 50 mL of hexane solvent was added. The sample was subjected to temperatures of 120°C for 20 minutes. After being treated the vial was allowed to cool down to 30°C before it was opened, and the hot solvent was then filtered using vacuum filtration to separate any suspended solids. The solvent containing the dissolved compounds was then placed in a rotatory evaporator at a temperatures of 30°C under vacuum to evaporate the hexane leaving behind the extracted bio-oil compounds. The hexane used for the extraction was recovered in the rotary evaporator and could be used for additional extractions.

3.2.2 Column Chromatograph

The method of column chromatography is used to separate compounds based on their polarity. Polar compounds, such as molecules containing oxygen or nitrogen that contain extra electron pairs, will be attracted to other polar compounds by electro-static attraction. Neutral compounds such as hydrocarbons do not have an electric dipole due to the charge being balanced throughout the molecule.

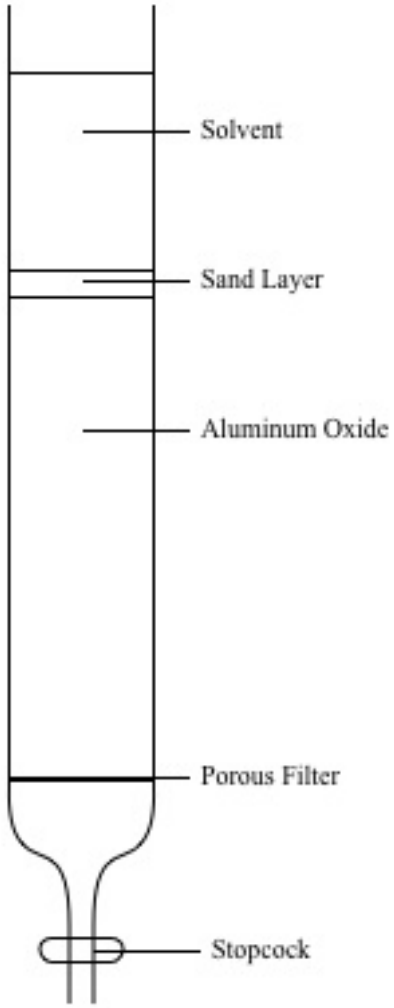

Figure 3.4: Alumina Column

The solid phase within the column is aluminum oxide (Al_2O_3) with a particle diameter of 5 m. 100 g of Al_2O_3 was mixed with 1 L of hexane to form a slurry and this was poured into the column using a funnel. The stopcock was left open, allowing solvent to drain into a beaker and keeping a flow through the column; this assisted the material in settling and forming a solid packed phase. Once the solid material was settled, approximately 10 g of dry sand was placed in the top of the column to form a barrier between the solid material and the solvent head above; 2 g of extracted bio-oil was then added to the sand layer using a pipette.

The stopcock of the column was opened half-way, allowing the solvent to drip into

the collection beaker at approximately 1 drop/s; this was done to keep solvent flowing through the column and ensure the solid phase was packed. Additional solvent was slowly added to the top of the column until the head was approximately 10 cm. Keeping the flow of solvent moving through the column prevented the sample from diffusing into the solvent above it.

The stopcock was then opened fully and one 100 mL sample jar of solvent was collected; this initial solvent was reused as it would not contain any compounds. Additional solvent was added to the top of the column to maintain the head and samples were collected until 4 100 mL sample jars were full.

The solvent from each jar was then evaporated using a rotary evaporator connected to a vacuum source. The evaporated solvent was condensed and collected in a recovery bulb while the sample was dried. Once solvent had been almost completely evaporated another jar was poured in and the sample allowed to dry until all the jars had been evaporated. The solvent was saved for other processes and the recovered sample was the upgraded bio-oil.

3.3 Analysis of Upgraded Bio-oil

The samples were analyzed at Agriculture Canada using Fourier transform infrared spectrometry (FTIR), nuclear magnetic resonance (NMR), gas chromatography with mass spectrometry (GC-MS). Pyrolysis field ionization mass spectrometry (Py-FIMS) was performed at the University of Rostock. The methods mentioned above with the exception of Py-FIMS provided qualitative data on the bio-oil composition. Py-FIMS analysis provided a quantitative analysis of the fuel which was required for computational modeling.

3.3.1 Py-FIMS Analysis

Analysis of the refined bio-oil sample by pyrolysis field ionization mass spectrometry (Py-FIMS) was performed by Dr. Gerald Jandl at the University of Rostock in Germany. The process of pyrolysis field ionization mass spectrometry heats a sample at a linear rate in

a quartz oven under high vacuum to a temperature of approximately 500°C. An electric field ionizes the vapors produced and the molecular ions enter a mass spectrometer where they are analyzed.

The resulting data contained the molecular mass in Daltons and the detector response for roughly 500 different molecular masses. These had been separated into the following categories: i) Carbohydrates, ii) Phenols & Lignin Monomers, iii) Lignin Dimers, iv) Lipids, v) Alkyl Aromatics, vi) Heterocyclic Nitrogen Containing Compounds, vii) Sterols, viii) Peptides, ix) Suberin, x) Free Fatty Acids, xi) 13C Signals and M+1 peaks (ISOM+1). The analysis showed no evidence of furans in the refined fuel.

The detector response was normalized to a sample size of 1 μL, and each of the individual masses from 1 to 500 Daltons was listed with the response. A mass spectrum database was used to determine the identity of many of the compounds. A summary of the analysis is given in 3.1; the raw data appear in Appendix B.

The number and types of compounds in these categories can be broad: for example, the lipids category contains alkanes and alkenes as well as other hydrocarbons. For modeling purposes this was broken down into more manageable categories. Table 3.1 contains alkanes, alkenes and alkyl-benzenes separated into their own categories. The response for cholestene was large and therefore it was separated into its own group. The results of the Py-FIMS analysis had duplicate entries for a substantial number of compounds, which is why the numbers in Table 3.0 add up to more than 100%.

3.3.1.1 Development of composition for modeling purposes The proportions of sterols and cholestenes were also far too high, partly as a result of these duplicate entries. Analysis for samples of unrefined bio-oil given by Schnitzer et al. (2007b) show only 0.1% sterols and cholestene. The refined fuel is about 10% of the original mass of heavy fraction, so if one assumes that all of the sterols in the unrefined oil are retained in the refined product, the sterol and cholestene concentration should only be about 1%. The duplicates and the sterol and cholestene excesses were therefore re-assigned, and the

Category	Mole Fraction in Refined Bio-oil (mol %)
m\z <56	0.34%
Carbohydrates	0.02%
Phenols, Lignin	0.09%
Lignin Dimers	4.52%
Lipids	18.56%
Alkyl-benzenes	3.97%
Heterocyclic N	0.59%
Sterols	31.82%
Peptides	0.04%
Suberin	0.91%
Fatty Acids	10.92%
ISOM+1	14.12%
Alkanes	12.2%
Alkenes	8.39%
Cholestene	8.92%
Unidentified	16.25%
Total	131.66%

Table 3.1: Mole Fraction of Detected Compounds from Py-FIMS Analysis

results from the Py-FIMS analysis were reduced to the following five major groups of compounds: i) n-paraffins, ii) alkenes, iii) fatty acids, iv) alkyl-benzenes and v) diols. These will later be used to describe the fuel for computational modeling purposes.

Sterols and cholestenes were re-distributed as 1.4% sterols, 12% n-diols, 12% n-alkanes, 10.4% 1-alkenes, based on comparisons with proportions of these compounds reported by Schnitzer et al. (2007b). The unaccounted category which contains unknown compounds, ISOM+1 and lipids was broken down into 12.0% alkyl-benzenes, 2.1% fatty acids, 11.6% alkenes and 6.9% unaccounted. Contributions from groups m/z 15-56, suberin, carbohydrates, lignin and NCOMP are small and were ignored (Hallett, 2013). The resulting composition for modeling purposes is given in table 3.2.

Group	Mole Fraction	Normalized	Molecular Mass Range: (kg kmol)	Corresponding Carbon Numbers
Alkanes	0.2420	0.2533	260-450	C17-C30
Alkenes	0.3034	0.3176	250-450	C18-C32
Alkyl-benzenes	0.16	0.1674	210-480	C16-C34
Fatty Acids	0.13	0.1361	250-460	C20-C30
Diols	0.12	0.1256	300-450	C20-C30
Neglected Species	0.0445	-	-	-
Total:	0.9999	1.0	-	-

Table 3.2: Mole Fraction and Normalized Fraction for Chemical Families

The length of the carbon chain between groups is roughly the same as well as the corresponding range of molecular weights. Only a very small amount of compounds is suspected to have molecular masses smaller than 210 kg/kmol.

4 Experimental

Droplet evaporation tests were performed on the fuel droplets to study their evaporation characteristics. Droplet temperature measurements were also performed to produce an approximate distillation curve, allowing the composition of the fuel to be deduced.

4.1 Droplet Evaporation Testing

Droplet evaporation experiments were performed using the suspended droplet / moving furnace technique, in which a single droplet suspended on a quartz fibre is rapidly heated in an environment of a predetermined temperature by moving a preheated furnace over the droplet (figure 4.5). During evaporation the temperature and size can be recorded and the results used to predict the fuel properties.

The furnace is heated electrically using a heating element connected to a controller. A thermocouple inside the furnace measures its temperature and the results are displayed on a digital readout. An atmosphere of nitrogen gas is maintained in the furnace enclosure to prevent droplet ignition, allowing pure droplet evaporation without chemical reaction. After each experiment the fuel vapours in the furnace are purged out by a flow of fresh nitrogen. Any residue left on the droplet support was burned off with a candle before conducting another experiment.

To conduct an experiment the furnace is moved pneumatically by opening and closing a series of valves connected to a high pressure nitrogen tank through a regulator. When the valve is opened a pneumatic cylinder pushes the furnace towards the suspended droplet and a small shutter is mechanically opened, allowing the droplet to enter. The furnace contains two windows on either side which allows the optical system to record the droplet behavior. A trigger switch on the furnace starts the stopwatch as soon as the furnace slides over the droplet.

4.1.1 Optics

A system of optics shown in figure 4.5 below allows a video of the droplet to be recorded as it undergoes evaporation while also keeping the image of a stopwatch in the same frame to record the time at which the events occur. The optical system consists of a video camera, 2 lenses, one prism and a light source. The light source is positioned behind the droplet and a lens focuses the image onto a plane in front of the camera; this plane is then imaged by the camera lens. Another lens focuses the image from the stopwatch through a prism and onto the same plane, which blends it with the first image of the droplet, resulting in both the droplet and stopwatch being visible in the same frame. The video is recorded on a computer using a hardware video acquisition card, and saved for analysis.

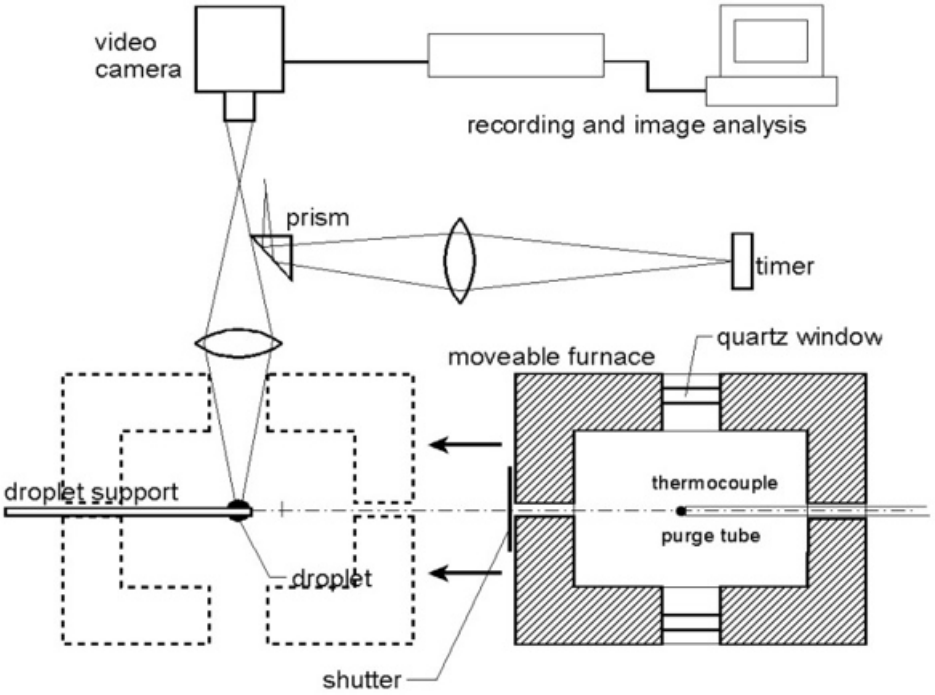

Figure 4.5: Sketch of Experimental Apparatus

Figure 4.6 shows a droplet suspended on a quartz fibre before the start of evaporation,

after the drop had been immersed in the furnace, and the bare fibre after the droplet had fully evaporated. Visible on the left hand side is the frame of the stopwatch showing the time elapsed after the droplet entered the furnace. Because the optics used inverted the images, these images were flipped vertically to be viewed correctly.

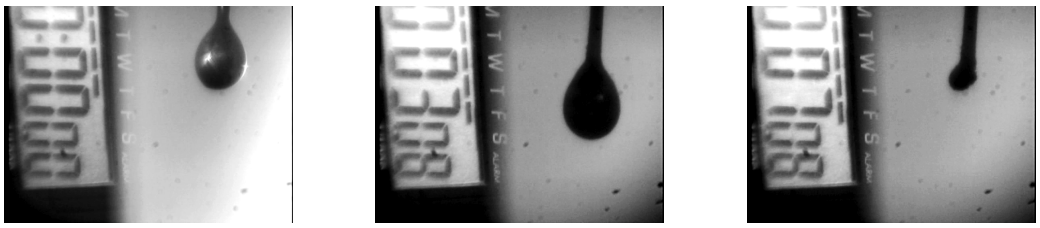

Figure 4.6: Images of Suspended Droplets

4.1.2 Data Analysis

Using the raw video captured from each test, a series of still frames was extracted at half second intervals, starting at 0 sec. and continuing until the droplet had fully evaporated. Each frame was analyzed using the Gimp photo editor. To determine the size of the droplet, the droplet was assumed to be a prolate spheroid in shape. An ellipse was drawn which provided a best fit to the droplet image and the height and width of the ellipse was recorded in pixels.

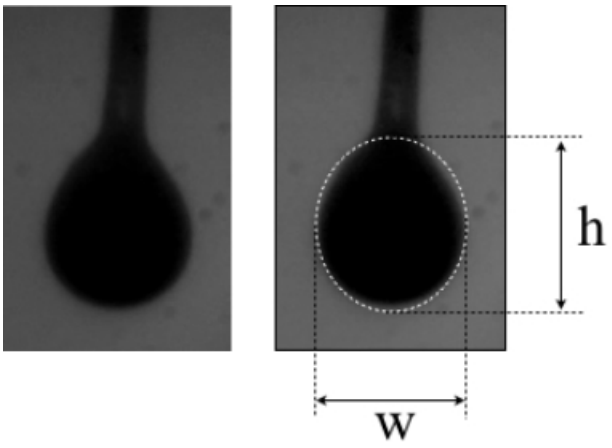

Figure 4.7: Ellipsoid Droplet Approximation

To calibrate the images, a scale was placed in the plane of the fibre bead and several

still frames from the video were taken. The horizontal and vertical distance was measured and averaged, and the calibration factor was then determined by dividing the pixel measurement by the distance on the ruler. The height and width could then be converted to millimeters.

$$h_{mm} = \frac{h_{px}}{f_{px/mm}} \tag{4.1}$$

$$w_{mm} = \frac{w_{px}}{f_{px/mm}} \tag{4.2}$$

The droplet was approximated as a prolate spheroid and its volume was determined using the following equation with the height and width measured from the droplet:

$$V = \frac{4}{3}\pi \left(\frac{h}{2}\right)\left(\frac{w}{2}\right)^2 \tag{4.3}$$

The diameter of the equivalent spherical droplet with the same volume was then calculated as follows:

$$d = 2\left(\frac{3}{4}\frac{V}{\pi}\right)^{\frac{1}{3}} \tag{4.4}$$

The volume of the droplet can also be determined from the volume of liquid as measured by the microliter syringe used to generate the droplets. The droplet volume is the volume of the liquid plus that of the fibre bead (small), and the diameter of the bead can be calculated from the video frames or measured with a micrometer. This served as a check on the accuracy of the droplet scaling.

4.1.3 Droplet Temperature Measurements

To measure the droplet temperature during vaporization a K-type wire thermocouple with 0.125 mm (0.005") leads was used in place of a quartz fibre as the droplet suspension for some experiments. A small bead of furnace cement 0.6 - 0.8 mm in diameter was placed on the thermocouple junction as a support for the droplet. A section of ceramic tube with two small holes down its length was used to insulate the thermocouple wires; this also provided a support allowing the thermocouple system to remain stable during the experiment. Figure 4.8 below shows a diagram of the suspended droplet and a photo of an actual droplet from experiments.

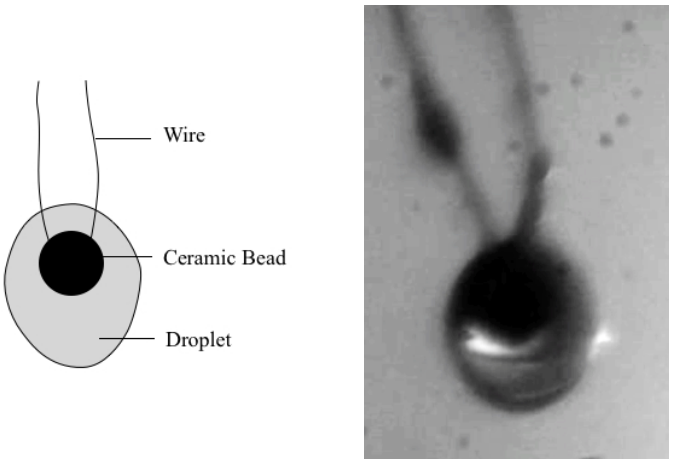

Figure 4.8: Droplet Suspended on a Wire Thermocouple

Since the thermal conductivity of the wire is considerably larger than that of quartz, heat from the furnace will be conducted into the interior of the droplet, increasing the rate of evaporation. To account for this a heat conduction term (Q_{wire}) is introduced as shown in equation 4.5:

$$Q_{wire} = 2\lambda_{wire} A_{wire} \left(T_\infty - T_R\right) / \delta \tag{4.5}$$

$$\lambda_w = 17.08 + 0.0189T \tag{4.6}$$

where λ_{wire} is the thermal conductivity of the wire in W/mK and A_{wire} is the cross sectional area, the factor of 2 accounts for each wire lead, and δ is the thickness of the boundary layer through which heat conduction is assumed to occur. Temperatures T_∞ and T_R are the furnace and droplet surface temperature respectively; the T used in equation 4.6 is the average of these two temperatures.

The values for the boundary layer thickness was determined to be 3.5 droplet radii from previous experiments comparing the evaporation of n-dodecane droplets on quartz fibres and thermocouples. The net effect of the thermocouple was shorter droplet lifetimes by approximately 20%.

The temperature and time was recorded on a computer using LabVIEW$^{\text{TM}}$ software allowing later analysis of the information. A trigger switch on the furnace was used to start the timer as soon as the furnace enclosed the droplet. The temperature measurements performed on the fuel droplets were recorded to support later analysis.

5 Computational Model

The results from the droplet evaporation tests were compared to a computational model of droplet evaporation which uses the method of continuous thermodynamics to describe the fuel. The fuel is modeled by separating it into several individual chemical families, each described by a distribution function. A number of transport properties - specific heat, thermal conductivity, diffusivity and others - are needed for the model and must be provided in the form of simple correlations with species molecular mass and temperature. These were developed from the properties of representative individual components in each family. Many of the compounds identified in the fuel do not have tabulated properties determined experimentally. To determine these properties several group contribution methods were used and the results from each compared to available experimental data; the properties used in the model were solely from the prediction methods.

5.1 Classical Droplet Evaporation Theory

The progress of droplet evaporation can be described using classical droplet evaporation theory. The heating, evaporation and combustion of most liquid fuels occurs in clouds of droplets; therefore, to understand this behavior one first needs to understand the processes of droplet evaporation.

A droplet suspended in a hot inert atmosphere undergoes heat and mass transfer. The net effect of these processes is a net flux of vapour away from the droplet surface as evaporation takes place and a net flux of heat to the droplet surface. Heat and mass transfer are closely coupled and a change in one will affect the other. An increase in the heat flux will cause an increase in the rate of evaporation. This increased mass flux, however, will reduce the heat flux into the drop and lower the rate of evaporation. Since these processes are both self-regulating, an equilibrium will be established.

The initial phase is called the transient heating phase; the mass flux is small and heat conducted to the droplet is primarily used to raise its temperature. As the mass

flux increases the heat flux decreases, and the point at which the temperature reaches a steady state is called the equilibrium vaporization temperature. At this point the heat transfer balances the rate of mass vaporization.

Multicomponent fuels have a similar behavior to that of pure fuels with some exceptions. As lighter compounds boil off, droplet temperature will rise, corresponding to the higher boiling temperature of the remaining heavy compounds. With some fuels containing very heavy compounds pyrolysis can take place before their boiling temperature is reached, which will result in the formation of a solid residue (Hallett and Clark, 2006).

5.2 Continuous Thermodynamics

Continuous thermodynamics treats a mixture of discrete compounds as a continuous distribution function defined by a mean and a standard deviation. Numerous discrete compounds with individual molecular weights are replaced with a continuous function over the range of molecular weights which best approximates the mixture.

The most common distribution function assumed is the gamma distribution, previous studies have shown a good fit to the composition of fuels (Hallett, 2000; Hallett and Clark, 2006). A gamma distribution is defined by two parameters, its distribution mean θ and standard deviation σ. The equation for the gamma distribution is shown below (equation 5.1) as a function of x with parameters α and β:

$$g(x) = \beta^{\alpha} \frac{1}{\Gamma(\alpha)} x^{\alpha-1} e^{-\beta x} \tag{5.1}$$

The distribution origin is assumed to be 0. The relationship between the mean θ and standard deviation σ are related to the values of α and β according to the following equations:

$$\alpha = \frac{\theta}{\beta} \tag{5.2}$$

$$\beta = \frac{\sigma^2}{\theta} \tag{5.3}$$

Figure 5.9 below shows a sample actual distribution of discrete compounds ranging in masses from approximately 230 to 500 g/mol and its corresponding cumulative distribution. Discrete data are first normalized so that the sum of the components is equal to 1.

$$\int_0^\infty g\left(x\right) = 1 \tag{5.4}$$

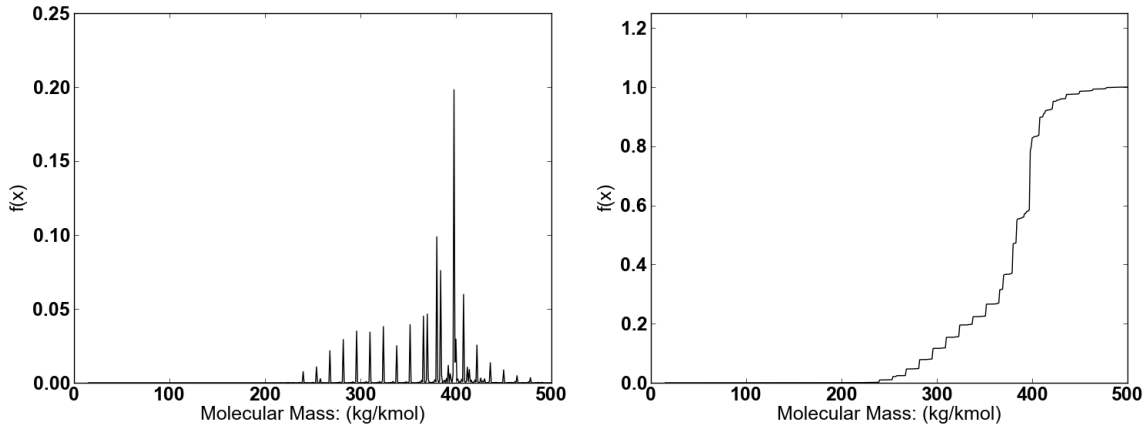

Figure 5.9: Discrete and Cumulative Data for Alkanes Present in the Fuel

The equivalent continuous distribution which represents this is shown in figure 5.10.

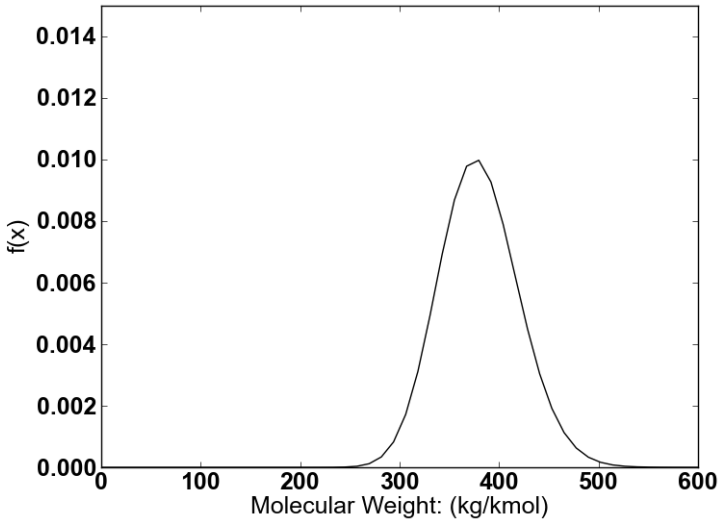

Figure 5.10: Gamma Distribution of Alkanes Present in the Fuel

The successful use of continuous thermodynamics to model complex fuels was demonstrated by Hallett and Beauchamp-Kiss (2010) in work with alcohol/fuel oil mixtures. The distribution parameters were chosen based on data from an ASTM distillation test of the mixture (Hallett and Beauchamp-Kiss, 2010).

5.3 Droplet Evaporation Model

A quasi-steady droplet evaporation model using continuous thermodynamics was developed in earlier work by Hallett (2000) and Hallett and Clark (2006) to model the evaporation characteristics of complex fuels. It was originally applied to droplet tests in which a single droplet was suspended on a fibre and then immersed in a furnace containing nitrogen. The quasi-steady approximation is used to treat systems at a steady-state when in actuality there can be some deviations. If these deviations from steady-state are small, as with the conditions of our experiments this approach is valid. As droplet evaporation occurs the fields of temperature and concentration will change. The rate at which they change is rapid compared to the overall process and therefore the process is said to be occurring at a quasi-steady state (Hallett, 2000).

Analytical solutions similar to classical droplet evaporation theory are performed to determine the gas phase concentration and temperature distribution and the evaporation rate. The energy and mass balances on the liquid phase are solved numerically as described in Hallett (2000). The model assumes a quasi-steady vapour phase in which the mass diffusion rates do not change considerably with time; this assumption is considered valid due to low pressure. Also assumed are constant transport properties for the species considered and no chemical reactions (Hallett 2000; Hallett and Clark 2006). The properties of the model remain uniform in space and variable in time and the changes are computed throughout the droplets lifetime. A spherical coordinate system is used for the calculations since the assumption is made that the droplet can be approximated by a sphere (Hallett and Clark, 2006).

The model also allows for compensation of heat transfer to the droplet through the thermocouple as described earlier, allowing fine-wire thermocouple experiments to be predicted.

5.4 Model Operation

The computational model was available in the Fortran language. To change operating conditions and properties new data files could be added and the code then recompiled. Calculations were run using Lahey Fortran 95 for MS Windows and gcc for Mac OSX.

A program called 'PROPTEST.FOR' was developed to check the individual input files for each chemical family to ensure the properties being calculated were done correctly. The input file in the program could be changed for each file and then the program compiled and run; the output properties were then compared with the correct values to check their validity.

5.4.1 Inputs

The input data are supplied to the model using several text files, one file for the properties of each chemical family and one for the environmental conditions (droplet size, furnace

temperature, etc.). Each of the files for the specific chemical families contains the coefficients for correlations which are used to calculate the values for the properties as they vary with molecular weight and temperature. Each file contains the '.DAT' extension and is named for the family which it represents: for example, the values for alkanes are stored in the 'ALKANES.DAT' file.

The environment settings are stored in 'MDOPCONS.DAT'. This file contains the environmental properties, initial liquid temperature of the droplet, furnace temperature and droplet radius. Also included are settings for the time step, time limit and other parameters which can be used to fine tune the model. Flags to switch on or off calculations for convection and thermocouple compensation are also present, along with the physical properties for heat transfer through the thermocouple wires. The details regarding thermocouple compensation are described in section 4.1.3.

5.4.2 Outputs

The model outputs data to text files which list the droplet diameter, temperature, composition and other properties as functions of time. It also includes a list of the properties which have been used in the calculations and the chemical family composition. The data can be imported into a spreadsheet and analyzed.

5.5 Distribution Functions

The group composition used in the model was developed using the Py-FIMS data obtained from Agriculture Canada and modified by Hallett (2013). Five major chemical families were identified; i) n-paraffins, ii) 1-alkenes, iii) n-alkyl fatty acids, iv) n-alkyl-benzenes and v) n-diols.

A cumulative gamma distribution curves were then fitted to the data so that it minimized the sum of squares of the deviations between the measured analysis and the distribution function, providing the best fit. This was done and the resulting values for the mean and standard deviation are listed in table 5.3. Plots of the gamma distribution

for each chemical family are shown in figure 5.11.

Group	Mean	Standard Deviation
Alkanes	380	40
Alkenes	380	50
Alkyl-benzenes	380	40
Fatty Acids	390	18
Diols	395	15

Table 5.3: Standard Model (5 Fractions) - Mean and standard deviations for the distribution functions used for each chemical family.

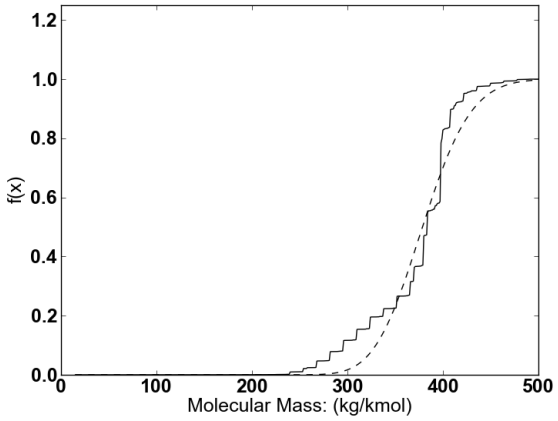

(a) Alkanes

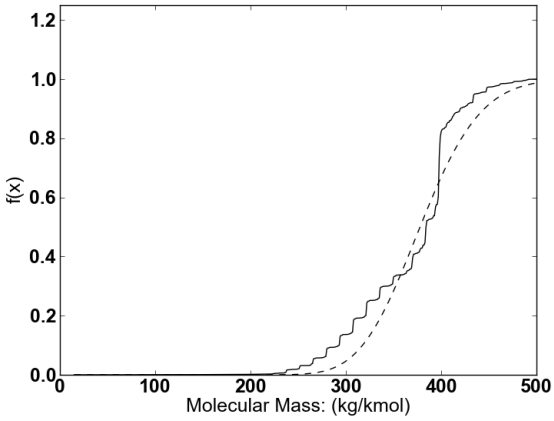

(b) Alkenes

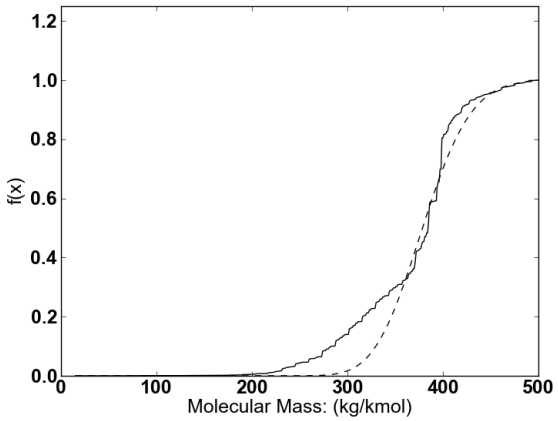

(c) Alkyl-benzenes

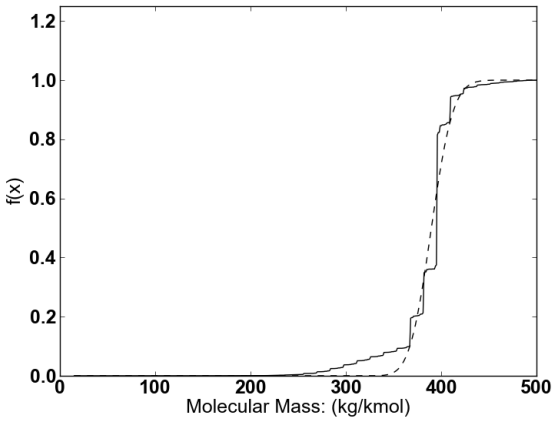

(d) Fatty Acids

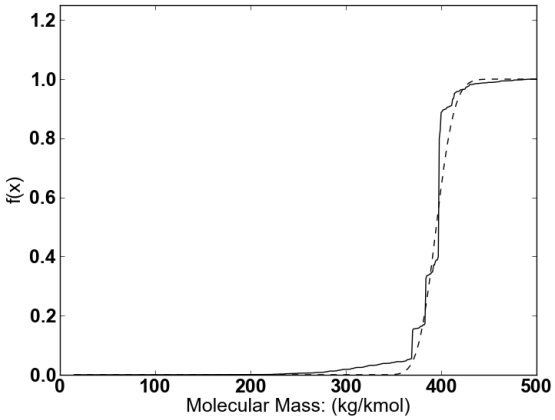

(e) Diols

Figure 5.11: Standard Model (5 Fractions) - Plots of cumulative discrete data (Solid Line) and fitted cumulative gamma distribution (Dashed Line) for the 5 fractions model showing fit.

It was also found that the fit could be improved by separating some of the groups

into a light and heavy fraction. When distribution functions were fitted to these a better fit was obtained. This increased the total number of distribution functions from 5 to 8. The values obtained for the mean and standard deviations of the groups separated are shown in table 5.4 below and plots of the gamma distributions are shown in figure 5.12. The graphs show the light and heavy fractions plotted together.

Group	Mole Fraction	Mean	Standard Deviation
Light Alkanes	0.05	295	25
Heavy Alkanes	0.24	390	22
Light Alkenes	0.09	300	30
Heavy Alkenes	0.21	395	25
Light Alkyl-benzenes	0.05	300	35
Heavy Alkyl-benzens	0.12	395	25
Fatty Acids	0.13	390	18
Diols	0.12	395	15

Table 5.4: Extended Model (8 Fractions) - Mean and standard deviations for the distribution functions used for the 8 fraction model of chemical families.

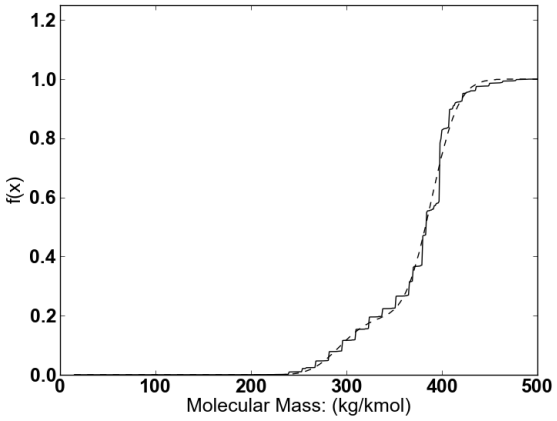

(a) Alkanes

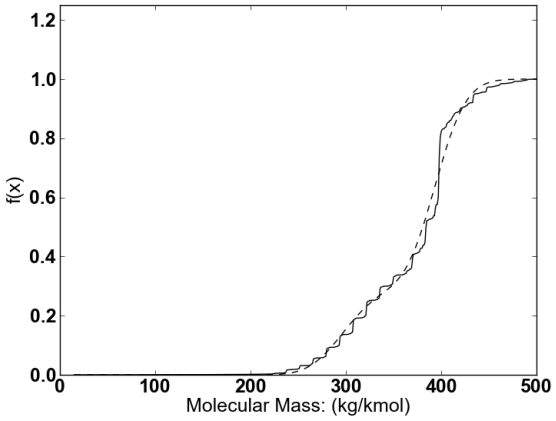

(b) Alkenes

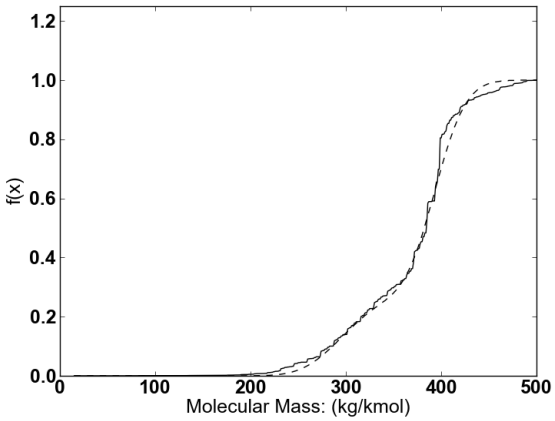

(c) Alkyl-benzenes

Figure 5.12: Extended Model (8 Components) - Plots of cumulative discrete data (Solid Line) and fitted cumulative gamma distributions (Dashed Line) for the 8 fraction model showing fit. Distributions for the fatty acids and n-diols are identical to those in the 5 fraction model.

Since the distributions are quite similar a simplified model consisting of only two distribution functions can be used to describe the distribution for the fuel as a whole (ie. all chemical groups combined together). This contains only a light and heavy distribution and properties for alkanes were used. The values for the mean and standard deviation are shown in table 5.5 and plots of the distributions in figure 5.13.

Group	Mole Fraction	Mean	Standard Deviation
Light	0.22	300	30
Heavy	0.78	295	20

Table 5.5: Simplified Model (2 Fractions) - Mean and standard deviations for the distribution functions for the model using a single light fraction and a single heavy fraction for the fuel as a whole.

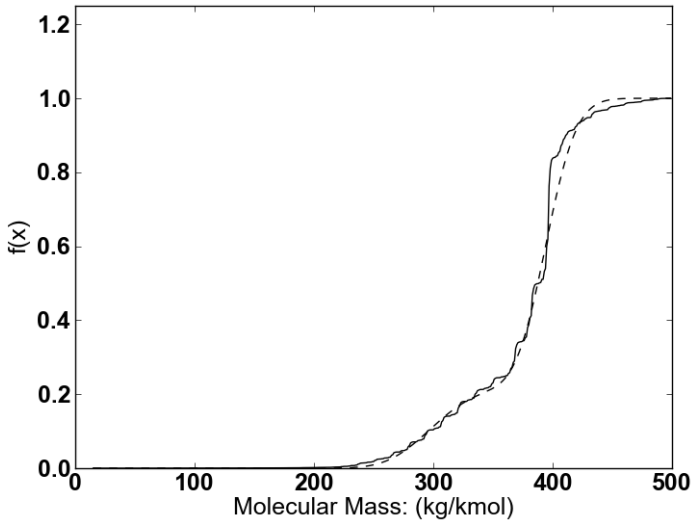

Figure 5.13: Simplified Model (2 Components) - Plots of cumulative discrete data (Solid Line) and fitted cumulative gamma distribution (Dashed Line) for the two fraction model showing fit.

5.6 Determination of Properties

To model the fuel, physical properties for its components must first be determined for the range of compounds present (approximately C_{16} to C_{32} for the present fuel) (Hallett, 2013). The continuous thermodynamics droplet model requires these properties in the form of fairly simple correlations which give the property as a function of molecular mass and temperature. To develop these, properties were first gathered for representative individual compounds in the desired carbon number range and the desired correlating equations were then fitted to these values. Few tabulated data are available for the high molecular mass compounds used here and therefore several group contribution meth-

ods were used to estimate these properties. Any available properties data were used to estimate the accuracy of the results obtained.

The physical data required for the model consist of a) critical temperature, pressure and volume, b) boiling point, c) enthalpy of vaporization, d) liquid specific heat, e) vapor specific heat, f) diffusion coefficients, g) thermal conductivity and h) liquid specific volume. Diffusivity and thermal conductivity were not predicted using group contribution methods but were calculated using Chapman-Enskog theory instead. The accuracy of each method will vary depending on the property we are interested in predicting. The properties prediction methods employed were those recommended by the standard properties reference work (Poling et al., 2001). To predict each of these properties compounds with carbon numbers ranging from C_{16} to C_{32} were selected, the number of hydrogen and oxygen atoms was determined for these carbon numbers and the molecular weight was calculated. Using a group contribution method the value for each compound was determined.

The method of Constantinou-Gani was used to predict the critical properties and boiling points, the method of Joback was used for enthalpy of vaporization and vapor specific heat, the method of Ruzicka-Domalski was used for the liquid specific heat and the method of Elbro for the liquid specific volume. To predict the diffusion coefficients and thermal conductivity Chapman-Enskog theory was used.

5.7 Group Contribution Methods

Group contribution methods provide a powerful means for the estimation of properties for compounds for which there are few or no available data. To predict these properties several different approaches are possible. Most methods use either groups, bonds or atomic contributions to calculate various properties (Poling et al., 2001).

In the case of group contributions, each group is assigned a weight for the property being predicted. A group is a simple arrangement of atoms which will contribute similarly to the total value of the property. Examples of common groups encountered in the

compounds of this work are -CH_3, CH_2, OH and COOH. Molecules are assembled using these simple groups and each group is assigned a weight for a particular property. The total value of the property is then determined as a function of the sum of products.

As an example, we can take n-dodecane, a simple n-paraffin, and break it down into two CH_3 and eight -CH_2- groups. The boiling point, for example, is determined by combining contributions for these groups according to the Constantinou-Gani correlation detailed in Section 5.7.2 (Table 5.6).

Group	Weight: (tb1k)	Number: (Nk)
CH_3-	0.8894	2
-CH_2-	0.9225	10

Table 5.6: Groups and Weights for Boiling Point Determination of Dodecane

$$T_b = 204.359 ln \left[\Sigma N_k \left(tb1k\right)\right] \tag{5.5}$$

$$T_b = 204.359 ln \left[2 \left(0.8894\right) + 10 \left(0.9225\right)\right]$$

$$T_b = 490.1 K$$

This is very close to the tabulated value of 489.5 K (Poling et al., 2001). Although fairly simple, these methods generally yield accurate predictions. The determination of the properties used in this thesis is outlined below.

5.7.1 Critical Values

The critical temperature and pressure for representative compounds in each chemical family were determined using the method of Constantinou-Gani (Poling et al., 2001). The following equations are used to calculate the critical temperature and critical pressure. Values of tc1k and pc1k are the weights for the individual groups for the critical temperature and pressure respectively. N_k is the number of each individual group.

$$T_{cr} = 181.128ln\left[\Sigma N_k\left(tc1k\right)\right] \tag{5.6}$$

$$P_{cr} = \left[\Sigma N_k\left(pc1k\right) + 0.10022\right]^{-2} + 1.3705 \tag{5.7}$$

The critical temperature and pressures were calculated for a range of compounds with carbon numbers from 16 to 32, and the results fitted to simple linear correlations for the variation of these properties with molecular weight.

$$T_{cr} = a_c + b_c M_i \tag{5.8}$$

$$P_{cr} = a_p + b_p M_i \tag{5.9}$$

Constants a and b were determined from a linear regression of the property and molecular weight. The values of tc1k are tabulated in (Poling et al., 2001). Values determined using this method are shown in appendix A.

5.7.2 Boiling Points

The boiling temperatures of representative species in each group were also determined using the method of Constantinou-Gani (Poling et al., 2001). The following equation is used to calculate the boiling temperature for the individual species:

$$T_b = 204.359ln\left[\Sigma N_k\left(tb1k\right)\right] \tag{5.10}$$

A linear correlation for the prediction of these properties as a function of molecular weight was then fitted as:

$$T_b = a_c + b_c M_i \tag{5.11}$$

Constants a and b were determined from a linear regression of the property and molecular weight. The values of tb1k are tabulated in (Poling et al., 2001). Values determined using this method are shown in appendix A.

5.7.3 Enthalpy of Vaporization

The enthalpy of vaporization was determined using the method of Joback (Poling et al., 2001), this method is similar to that of Constantinou-Gani, but different groups are used. The following equation is used to calculate the enthalpy for individual species in kJ/gmol K:

$$h_{fgi} = 15.30 + \Sigma \left[N_k \left(hvk \right) \right] \tag{5.12}$$

The value of hvk is the weight for each of the individual groups, and N_k is the number of these groups in the molecule. A linear correlation for the prediction of these properties as a function of molecular weight was derived in the following form:

$$h_{fgi} = \left[a_H + b_H M_i \right] \Phi_H \tag{5.13}$$

The constants a_H and b_H correlate the enthalpy of vaporization at the compounds boiling point. The Φ_H term is the widely-used Watson relation for the temperature dependence of hfg (Poling et al., 2001), and is expressed as:

$$\Phi_H = \left[\left(T_{cr} - T \right) / \left(T_{cr} - T_b \right) \right]^{0.38} \tag{5.14}$$

Critical and boiling temperatures previously calculated are used to estimate the value

of Φ_H. Tabulated values for the Joback coefficients are listed in (Poling et al., 2001).

5.7.4 Liquid Specific Heat

The liquid specific heat for individual compounds was calculated using the Ruzicka-Domalski method (Poling et al., 2001). The equation below is used, where a_L, b_L and d_L are coefficients determined by the group method:

$$C_{pL} = a_L + b_L T + d_L T^2 \tag{5.15}$$

These coefficients are determined for each species using equations 5.16 to 5.18 shown below. Each coefficient is equal to the sum of the products of the group weight (a_i, b_i, d_i) and the number of groups present (N_k).

$$a_L = \Sigma N_K a_i \tag{5.16}$$

$$b_L = \Sigma N_K b_i \tag{5.17}$$

$$d_L = \Sigma N_K d_i \tag{5.18}$$

Values of the specific heat are calculated in J/molK; since this is already expressed in terms of moles the correlating equation can be cast in the linear form shown in equation 5.19 below.

$$C_{PL} = \left(a_L + b_L T + d_L T^2\right) M_i \tag{5.19}$$

It was noticed that for the chemical families used there was only a small variation in the liquid specific heat expressed in mass units (kJ/kg K) with molecular mass. The

coefficients and values for the liquid specific heat are tabulated in appendix A, and group weights are available in (Poling et al., 2001).

5.7.5 Vapour Specific Heat

The vapor specific heat for each species was determined using the method of Joback (Poling et al., 2001):

$$C_{P^o} = A_i - 37.93 + [B_i + 0.210]\,T + [C_i - 3.9E - 4]\,T^2 + [D_i + 2.06E - 7]\,T^3 \quad (5.20)$$

The coefficients A_i through D_i used above are determined using equations 5.21 to 5.24 below, each coefficient is the sum of the products of the number of groups and the group weight.

$$A_i = \Sigma\,[N_k\,(C_pAk)] \quad (5.21)$$

$$B_i = \Sigma\,[N_k\,(C_pBk)] \quad (5.22)$$

$$C_i = \Sigma\,[N_k\,(C_pCk)] \quad (5.23)$$

$$D_i = \Sigma\,[N_k\,(C_pDk)] \quad (5.24)$$

A linearized form for the vapor specific heat as a function of molecular weight is shown in equation 5.25.

$$C_p = a_T\,(T) + b_T\,(T)\,M_i \quad (5.25)$$

The coefficients a_T and b_T are both functions of temperature and are each correlated as:

$$a_T = a_1 + a_2T + a_3T^2 + a_4T^3 \tag{5.26}$$

$$b_T = b_1 + b_2T + b_3T^2 + b_4T^3 \tag{5.27}$$

The coefficients a_1 to a_4 and b_1 to b_4 shown above are each determined by linear regression of equations 5.26 to 5.27. Values of the liquid specific heat calculated are listed in appendix A, groups for the method of Joback are available in (Poling et al., 2001).

5.7.6 Diffusion Coefficients

The diffusion coefficients for each species were determined using Chapman-Enskog theory (Poling et al., 2001) for a species diffusing into nitrogen gas. The diffusivity in cm^2/s was calculated for each species using equation 5.28.

$$D_{AB} = \frac{0.00266T^{3/2}}{PM_{AB}^{1/2}\sigma_{AB}^2\Omega_D} \tag{5.28}$$

The temperature T is measured in Kelvins, P is the pressure in bar, and M_{AB} is defined as the reduced molecular mass measured in g/mol;

$$M_{AB} = 2\left[\frac{1}{M_A} + \frac{1}{M_B}\right]^{-1} \tag{5.29}$$

where M_A and M_B are the molecular masses of species A and nitrogen respectively. The values ϵ and σ are called the characteristic Lennard-Jones energy and length respectively. Ω_D is the collision integral for diffusion and is a function of the non-dimensional temperature. Its value can be approximated using equation 5.30 (Poling et al., 2001).

$$\Omega_D = \frac{A}{(T^*)^B} + \frac{C}{exp\,(DT^*)} + \frac{E}{exp\,(FT^*)} + \frac{G}{exp\,(HT^*)} \tag{5.30}$$

$$where \quad A = 1.06036; B = 0.15610; C = 0.19300; D = 0.47635; \tag{5.31}$$
$$E = 1.03587; F = 1.52996; G = 1.76474; H = 3.89411$$

The non-dimensional temperature (T^*) is a function of Boltzmanns constant k, the absolute temperature and the Lennard-Jones interaction energy, it is determined as follows:

$$T^* = kT/\epsilon_{AB} \tag{5.32}$$

Values for the interaction values ϵ_{AB} and σ_{AB} were determined as follows:

$$\epsilon_{AB} = (\epsilon_A \epsilon_B)^{1/2} \tag{5.33}$$

$$\sigma_{AB} = \frac{\sigma_A + \sigma_B}{2} \tag{5.34}$$

The component values of σ and ϵ were determined from the critical properties using the correlation of Chung (Poling et al., 2001):

$$\frac{\epsilon}{k} = \frac{T_{cr}}{1.2593} \tag{5.35}$$

$$\sigma = 0.809 V_{cr}^{1/3} \tag{5.36}$$

Once the diffusivities are calculated for a range of molecular weights a correlation is

developed to calculate the diffusivity from the molecular mass and temperature:

$$D_i = [a_D + b_D M_i]\,\Phi_D \tag{5.37}$$

The temperature dependence of this equation is given by Φ_D which is based on the Sutherland equation for the variation of gas viscosity with temperature:

$$\Phi_D = \frac{T^{5/2}}{b_\Phi + T} \tag{5.38}$$

The value of b_Φ is optimized to provide the best fit to the values calculated for the representative individual species. This is done by first setting a trial value of b_Φ and calculating values of a_D and b_D. The resulting diffusion coefficients determined from the linear correlation (equation 5.37) are compared to the values from equation 5.38, and b_Φ is adjusted until the sum of squares of deviations from these values is minimized. Values for the diffusion coefficients calculated are listed in Appendix A.

5.7.7 Thermal Conductivity

The thermal conductivity is determined using the Eucken equation as modified by Stiel and Thodos (Poling et al., 2001):

$$\frac{\lambda M'}{\eta C_v} = 1.15 + \frac{2.03}{C_v/R} \tag{5.39}$$

M is the molecular weight in g/mol, is the viscosity in Pa s, is the thermal conductivity in W/mK and the constant volume heat capacity C_v is in J/kmol. The viscosity is determined using Chapman-Enskog theory:

$$\eta = \frac{26.69\,(MT)^{1/2}}{\sigma^2 \Omega_v} \tag{5.40}$$

where M is the molecular mass in g/mol, and T is the absolute temperature in Kelvins. The characteristic length is in Angstroms and is determined using the method of Chung (Poling et al., 2001):

$$\sigma = 0.809 V_c^{1/3} \tag{5.41}$$

The critical volume was calculated using the method of Constantinou-Gani. The viscosity collision integral Ω_v was calculated using the empirical equation of Neufeld (Poling et al., 2001):

$$\Omega_v = \left[A\left(T^*\right)^{-B}\right] + C\left[exp\left(-DT^*\right)\right] + E\left[exp\left(-FT^*\right)\right] \tag{5.42}$$

$$\begin{aligned} where \quad & A = 1.16145; B = 0.14874; C = 0.52487; \\ & D = 0.77320; E = 2.16178; F = 2.43787 \end{aligned} \tag{5.43}$$

The dimensionless temperature (T*) is:

$$T^* = \frac{kT}{\epsilon} \tag{5.44}$$

This and the collision integral are similar but not identical to those used to calculate the diffusivity. The thermal conductivity is then correlated with the molecular weight using equation 5.45 with temperature-dependent coefficients a_K and b_K.

$$\lambda_i = a_K\left(T\right) + b_K\left(T\right) M_i \tag{5.45}$$

Values of a_K and b_K are represented by a linear correlation with temperature:

$$a_K\left(T\right) = a_{KC} + a_{KT} T \tag{5.46}$$

$$b_K(T) = b_{KC} + b_{KT}T \tag{5.47}$$

The correlations for the thermal conductivity calculated are listed in Appendix A.

5.7.8 Liquid Specific Volume

The specific volume of the liquid was determined using the method of Elbro:

$$\nu_i = A_i + B_i T + C_i T^2 \tag{5.48}$$

Coefficients A_i, B_i and C_i, are determined using group contributions:

$$A_i = \Sigma\left[N_k a_i\right] \tag{5.49}$$

$$B_i = \Sigma\left[N_k b_i\right] \tag{5.50}$$

$$C_i = \Sigma\left[N_k c_i\right] \tag{5.51}$$

The values of a_i, b_i and c_i are the specific groups weights and N_k the number of each groups present. A linear correlation of the specific volume with molecular weight is shown below.

$$\nu_i = \left(a_v + b_v M_i\right)\left[1 + \alpha_P\left(T - 20\right)\right] \tag{5.52}$$

The specific volume is calculated at 20°C and the second term is a temperature correction factor which uses the isobaric expansion coefficient α_P and the temperature in Celsius. To determine α_P a trial value is first set and the mean square error of the correlation as compared to the values from the Elbro method; α_P is then varied until the

mean square error is minimized. The results are tabulated in Appendix A.

6 Results

The results from the droplet evaporation and temperature measurements are presented here along with a comparison to the computational model. These measurements were compared to the model to determine how accurately it was able to predict the temperature and evaporation profiles.

Immediately after a suspended droplet was inserted into the furnace it was observed to enlarge due to thermal expansion. During this period of heating the droplet was observed to remain stationary on the fibre, and only small disturbances were observed. As the temperature of the droplet approached the boiling points of its lighter components disruptions and internal boiling of the droplet was observed. In some cases micro-explosions were observed and this resulted in material being ejected from the droplet. This was only observed a few times and in all the trials used in this study, no material was observed to be ejected. During this period of boiling the droplet volume was observed to decrease due to evaporation. At the end of evaporation only a small amount of residue was observed to remain on the quartz fibre bead.

As an indication of the precision of the data, error bars are shown for all experimental measurements in this chapter; they represent plus and minus one standard deviation from the mean.

6.1 Droplet Temperature Measurements

Droplet temperature measurements were performed to determine the distillation characteristics of our fuel and to check the fuel composition used in our model. The amount of fuel available was too small for a standard ASTM D86 distillation test, but droplet temperatures provided equivalent information. During evaporation the droplet is in a quasi-steady state and this provides a good approximation to an actual distillation test.

Droplet evaporation tests using a fine-wire thermocouple were performed at various temperatures ranging from 300°C to 800°C at 100°C intervals. Five trials were performed

for each temperature and the results averaged. The standard deviation was determined from these trials and showed good repeatability.

The frames below show a droplet in various stages of evaporation at a temperature of 600°C; in each frame the time advances by 1 second. In the initial image the droplet is shown suspended on the thermocouple in ambient air, in the next three frames the droplet enlarges due to heating (thermal expansion), and after this stage the droplet size decrease quickly as the droplet evaporates.

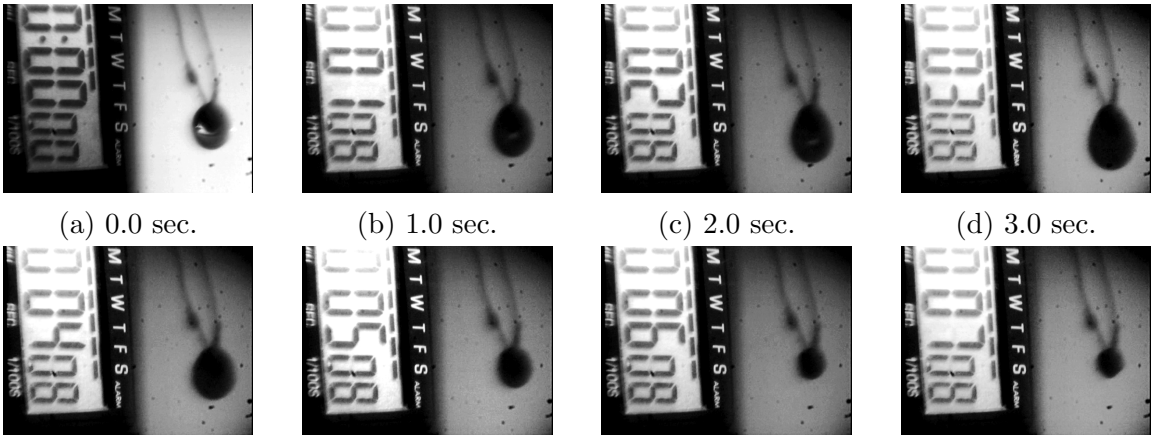

(a) 0.0 sec. (b) 1.0 sec. (c) 2.0 sec. (d) 3.0 sec.

(e) 4.0 sec. (f) 5.0 sec. (g) 6.0 sec. (h) 7.0 sec.

Figure 6.14: Video frames from 0 to 7 seconds of a droplet temperature test at 600°C

Shown below (figure 6.15) are temperature profiles for a fuel droplet evaporating at 300 and 400°C. In each case the temperature of the droplet rises quickly as it approaches the furnace temperature. At both of these temperatures small disruptions were observed, possible due to a variation in surface tension of the droplet causing the droplet to move a bit on the support. The slope of the temperature profile however was observed to change gradually, similar to that of a pure fuel.

A larger standard deviation was observed at 400°C, this could be the result of increased internal boiling however it was not observed at 500°C (figure 6.16) but was seen to occur at temperatures including and greater then 600°C (Figures 6.16 & 6.17).

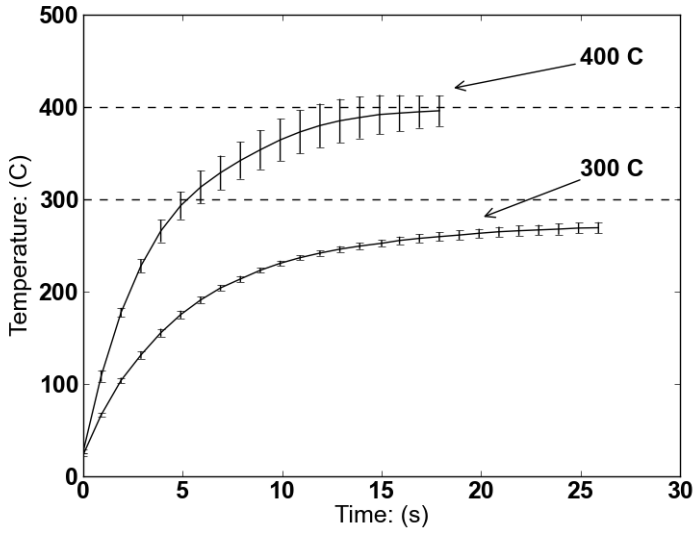

Figure 6.15: Measured droplet temperature as a function of time for a 1.6 mm droplet evaporating at 300 and 400°C. The furnace temperature for each trial is denoted by a dashed line. Error bars are drawn at plus and minus one standard deviation from the mean.

Since the profile showed a rapid increase with a plateau close to the furnace temperature it is believed that the bulk of the components had boiling temperatures which exceeded 300°C. When mixtures evaporate they show usually a steadily rising temperature not far below the bubble point (Hallett, 2000), corresponding to the rise in bubble point of the mixture occurring as a result of distillation during evaporation. The asymptotic approach to the furnace temperature in Fig. 6.15 suggests that at this point the mixture is well below its bubble point. During all the tests a residue was left on the surface of the thermocouple; however, it was most noticeable at 300°C, presumably because a higher percentage of compounds had boiling points greater than this.

Tests at 500°C and 600°C (figure 6.16) showed similar results to those seen at lower temperatures. It was however noticed that a slight change in the slope was detected above 400°C, indicating perhaps a transition from the boiling off of lighter compounds to that of higher boiling components. Data from both these temperatures show this characteristic slope change. The temperature still approaches the furnace temperature at the very end of the droplet lifetime. More comments will be made on this behavior when the data are

compared with numerical model predictions.

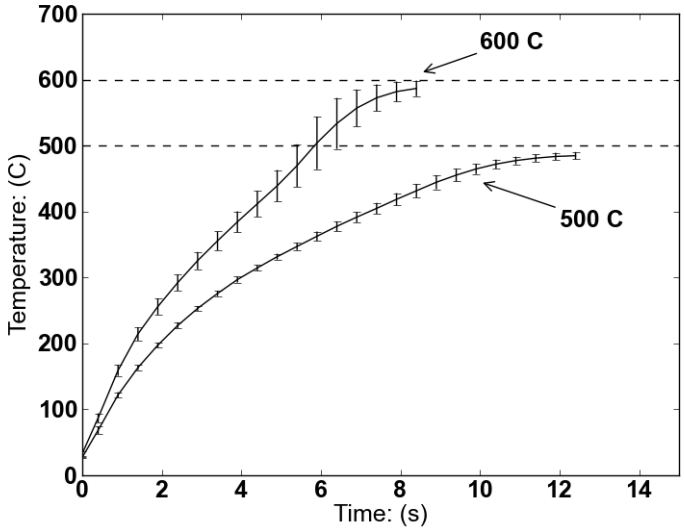

Figure 6.16: Measured droplet temperature as a function of time for a 1.6 mm droplet evaporating at 500 and 600°C. The furnace temperature for each trial is denoted by a dashed line. Error bars are drawn at plus and minus one standard deviation from the mean.

At 500°C there was excellent agreement between the different trials performed, and hence little scatter. At 600°C, towards the end of the droplet lifetime scatter was observed to become more noticeable. This was caused by the onset of vigorous disruption and bubbling of the droplet surface, which was observed at higher temperatures and is believed to indicate internal boiling of the lighter components of the mixture.

Observations at temperatures of 700 and 800°C (figure 6.17) showed more violent boiling and droplet disruption than was seen at lower temperatures. Towards the end of the droplet lifetime the standard deviation was observed to decrease; this coincides with the point at which the liquid has almost disappeared and the remaining evaporation is rapid. Towards the end of the droplet life the thermocouple bead starts to become exposed to the gases in the furnace. At this point the readings are no longer representative of the actual liquid temperature.

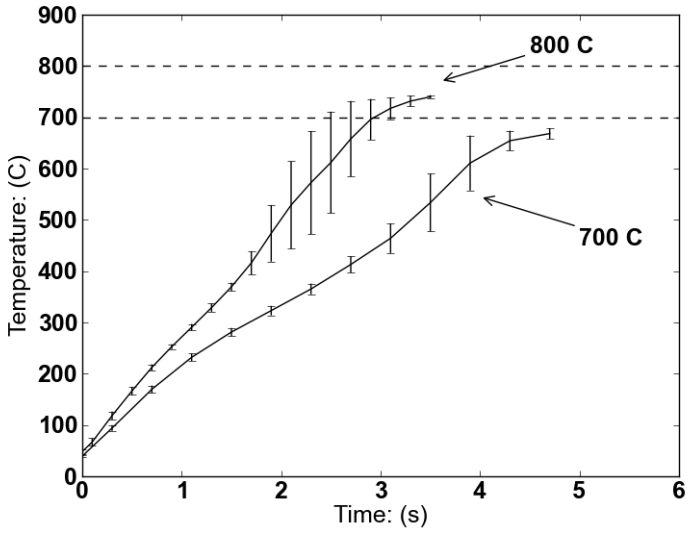

Figure 6.17: Measured droplet temperature as a function of time for a 1.6 mm droplet evaporating at 700 and 800°C. The furnace temperature for each trial is denoted by a dashed line. Error bars are drawn at plus and minus one standard deviation from the mean.

Luminous effects from the droplets were also observed at high temperatures and not at temperatures below 700°C. These are believed to be caused by the reflection of visible radiation from the walls of the furnace. The nitrogen atmosphere rules out any form of combustion from taking place. Shown below are droplets at approximately the same stage in the evaporation process at various temperatures. In the last two frames the thermocouple bead can be clearly seen inside the droplet.

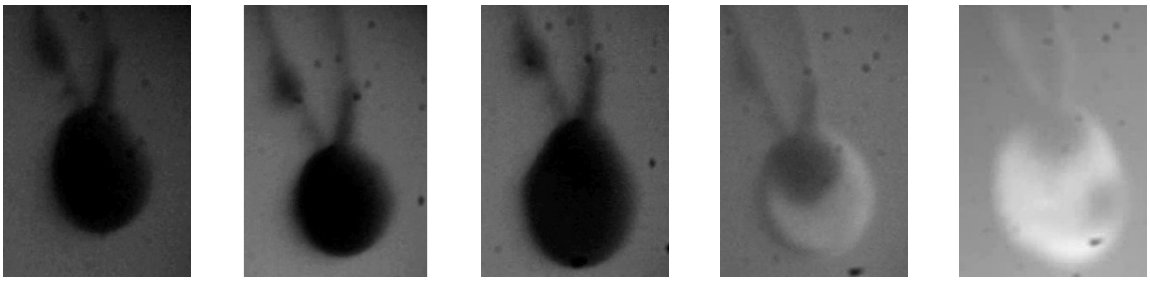

(a) 400 °C (b) 500 °C (c) 600 °C (d) 700 °C (e) 800 °C

Figure 6.18: Video frames of droplet luminosity at various temperatures

6.1.1 Comparison of Droplet Temperature Measurements to a Numerical Model

Profiles for each temperature were computed using the numerical model with thermocouple compensation turned on. The fuel properties used are from section 5.7 and the composition information used in the model is from table 5.3. The standard model (5 distributions) was used for the calculations presented here. Two other models are presented and compared in section 6.3.

Temperature profiles at 300 and 400°C (figure 6.19) were first compared to those of the model. In each case the shape of the curve closely approximated the experimental data (Figures 6.15 to 6.17). At 300°C the droplet lifetime was over predicted by almost a factor of 2, at 400°C the droplet lifetime was predicted almost exactly and in all other trials the droplet lifetime was under predicted. It was observed that there was a residue remaining on the bead after evaporation had taken place; this suggested that a small amount of material had not evaporated but instead underwent pyrolysis or polymerization and formed a solid residue. The original analysis has shown that high boiling point compounds such as sterols are present in small quantities; it is believed that these compounds might contribute to raising the liquid boiling point towards the end of the droplet lifetime and formation of residue.

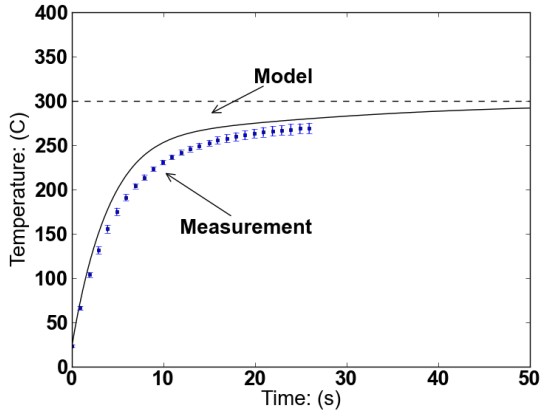

(a) $T_\infty = 300^oC$

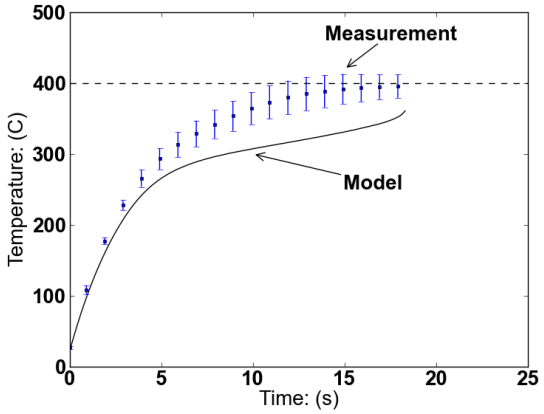

(b) $T_\infty = 400^oC$

Figure 6.19: Comparison of measured droplet temperature and model prediction at 300 and 400°C. The furnace temperature is denoted by a dashed line. Error bars are drawn at plus and minus one standard deviation from the mean.

At 400°C a better agreement between the experimental data and the model is observed. After 4 seconds a change in the slope of the model is observed indicating the transition from the transient heating phase to more or less quasi-steady evaporation. The droplet then disappears just before 20 seconds.

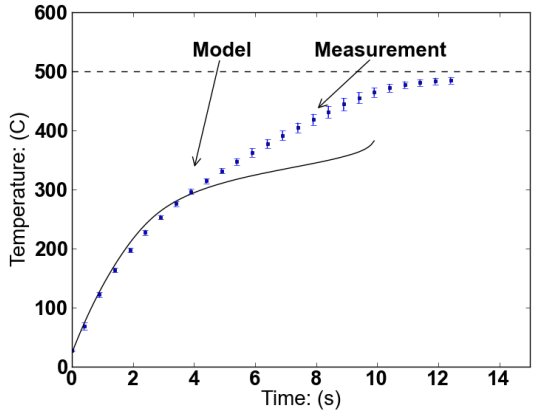

(a) $T_\infty = 500^oC$

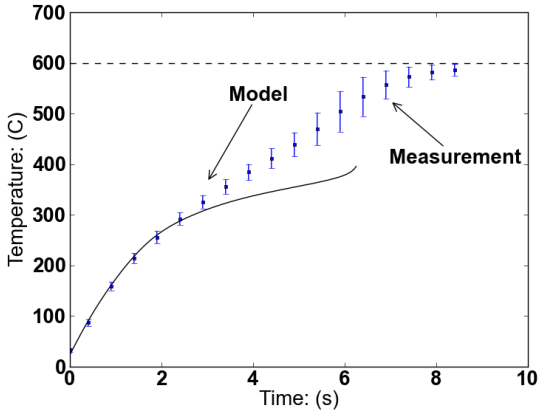

(b) $T_\infty = 600^oC$

Figure 6.20: Comparison of measured droplet temperature and model prediction at 500 and 600°C. The furnace temperature is denoted by a dashed line. Error bars are drawn at plus and minus one standard deviation from the mean.

At temperatures of 500 and 600°C similar results are obtained to those of 300 and 400°C. In each of these cases the shape of the curve closely approximates that of the

experimental data, with a droplet lifetime approximately 25% longer that of the model. The model predictions of the heating phase is very close to what is observed in the experimental results.

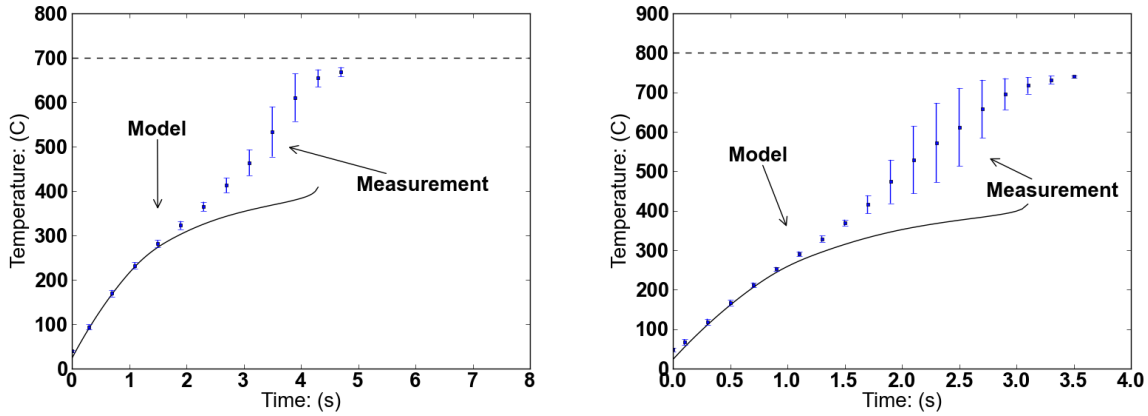

(a) $T_\infty = 700^oC$ (b) $T_\infty = 800^oC$

Figure 6.21: Comparison of measured droplet temperature and model prediction at 700 and 800°C. The furnace temperature is denoted by a dashed line. Error bars are drawn at plus and minus one standard deviation from the mean.

At 700 and 800°C similar results were obtained to those of the lower temperatures except more vigorous bubbling was observed to take place. Rapid changes to the droplet size and orientation took place which coincides to the times at which the deviation of the temperature increased. Based on this we can deduce that these droplet fluctuations affect the rate of heating.

According to the analysis of the fuel (table 3.2), the components range in molecular mass is from about 250 to 450 kg/kmol, and the properties correlations show that this corresponds to a component boiling point range of about 300 to 450°C. As expected, the predicted droplet lifetimes end at the top of this range of temperatures. The fact that this measured data continue beyond this point strongly indicates that a solid residue has formed which is simply undergoing transient heating until it reaches the furnace temperature: in other words, this part of the temperature record no longer has anything to do with liquid droplet behavior, and therefore is not captured by the model. It can be concluded therefore that the modeled liquid composition gives a good approximation to

measured droplet temperatures in the range in which the droplet is still liquid.

6.2 Droplet Vaporization Tests

Droplet vaporization tests were performed using a quartz fibre to support the droplet. Measurement of the droplet dimensions in successive frames of the video allowed the calculation of its volume, and from this its diameter as that of a spherical droplet of equal volume. The results of three trials were averaged. Shown below are droplets at various stages of evaporation.

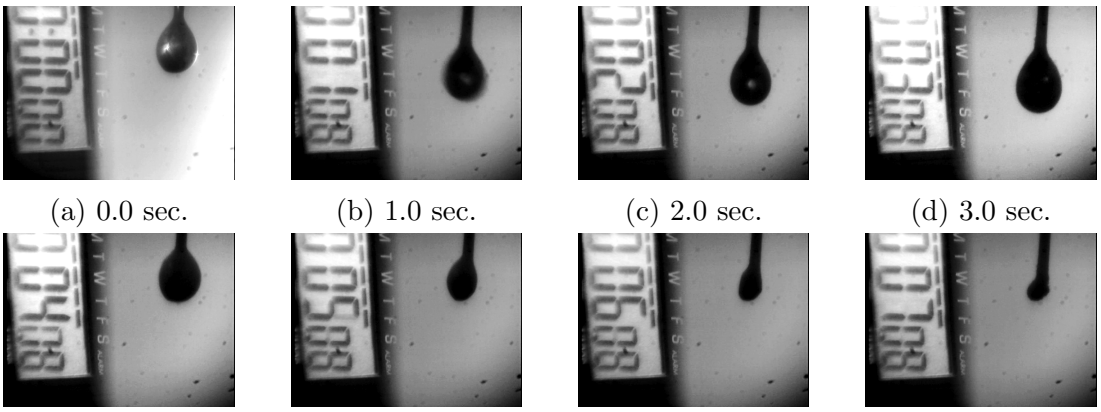

(a) 0.0 sec. (b) 1.0 sec. (c) 2.0 sec. (d) 3.0 sec.

(e) 4.0 sec. (f) 5.0 sec. (g) 6.0 sec. (h) 7.0 sec.

Figure 6.22: Droplets suspended on quartz fibre at times From 0 to 7 seconds at 600°C

Droplet evaporation tests on quartz fibers were performed at 500, 600 and 700°C and the results compared to predictions from a numerical model. In all of the trials some disruption and bubbling was observed and the droplet shape and orientation was observed to change rapidly during the evaporation phase.

At the end of the trials it was noted that the fibre bead was coated with a layer of carbon residue, caused by the pyrolysis of heavy compounds in the fuel. It was not possible to weigh the residue and therefore determine the percentage of fuel which evaporated. However, the size of the residue is evident from the fact that in all the experimental records shown the final diameter recorded is significantly greater than that of the fibre bead (which was about 0.6 mm).

Droplet evaporation testing was first conducted at a furnace temperature of 500°C (figure 6.23). Immediately after the furnace enclosed the droplet it was observed to grow due to thermal expansion; no bubbling was observed to take place at this point. At approximately 4 seconds bubbling and evaporation were observed to start (denoted by dotted line on figures). During this period the droplet size varied rapidly as it would grow and collapse. As the droplet approached the point of vanishing the fluctuations were observed to cease just before the droplet dissapeared.

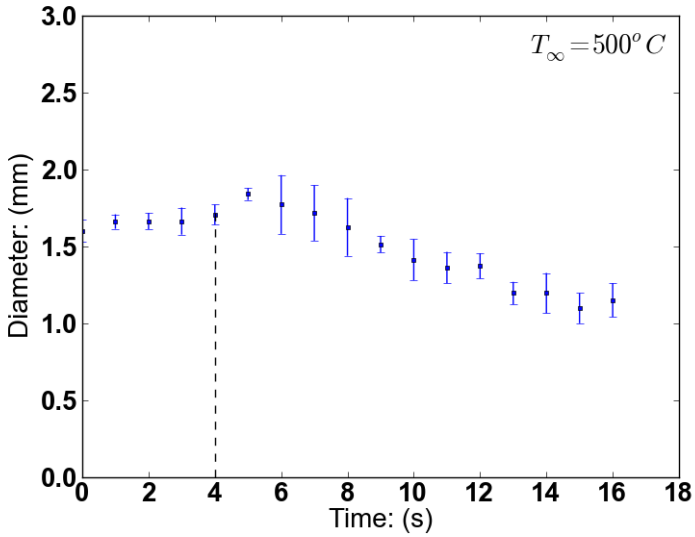

Figure 6.23: Measured droplet evaporation history at 500°C. Each point is the average of three separate experiments; error bars give the standard deviation. Dashed line indicates onset of disruptions.

The profile at 600°C (figure 6.24) is similar to that of the previous except with a shorter droplet life and quicker onset of bubbling and evaporation. This is expected behavior, as an increase in temperature will produce a larger heat flux. During the heating phase there was little growth of the droplet until boiling started which occurred at approximately 2.5 seconds. The droplet then rapidly enlarged and underwent disruptions as it evaporated.

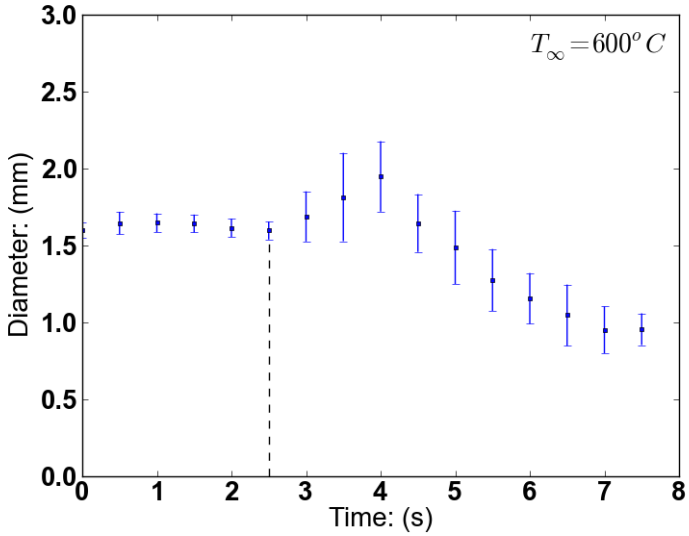

Figure 6.24: Measured droplet evaporation history at 600°C. Each point is the average of three separate experiments; error bars give the standard deviation. Dashed line indicates onset of disruptions.

At 700°C (figure 6.25) the same behavior was observed. A notable difference is the rapid onset of disruptions which occurred almost immediately after the droplet was exposed to the hot environment. The observed droplet diameter appears to enlarge after this, but this is largely a consequence of disruption and bubbling rather then thermal expansion.

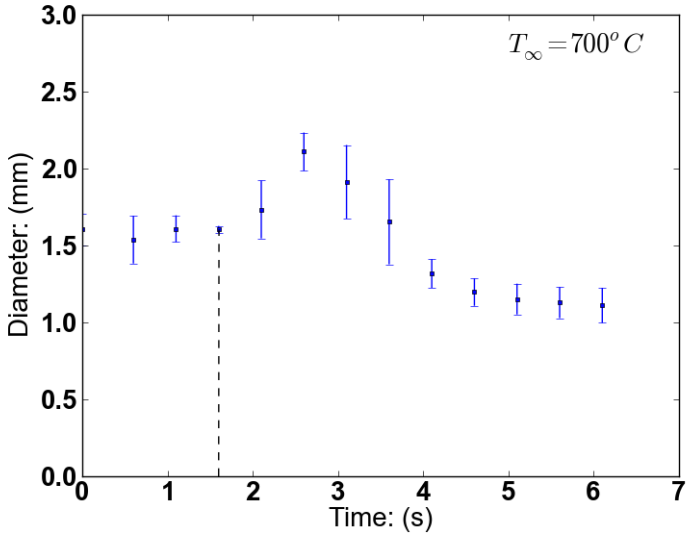

Figure 6.25: Measured droplet evaporation history at 700°C. Each point is the average of three separate experiments; error bars give the standard deviation. Dashed line indicates onset of disruptions.

6.2.1 Comparison of Droplet Vaporization Tests to a Numerical Model

Because of the multi-component nature of the fuel, it is not expected to behave as would be predicted using droplet evaporation theory for a single component droplet. The numerical model described in section 5.3 was used to make predictions for droplet evaporation using the fuel composition data. The model is unable to reproduce the effects of internal boiling and the rapid growth and shrinking behavior observed, but once this behavior ceases the model is once again expected to predict the behavior, provided that the disruption phase does not result in significant ejection of material from the droplet. If this was the case then the droplet diameter would be expected to decrease at a much higher rate then by evaporation alone. Careful analysis of the video frames does not show significant amounts of fuel being ejected.

In figure 6.26 below experimental data collected at 500°C was compared to the predictions of the model. The initial heating phase shows excellent agreement with the model; however, at the onset of disruption the model deviates, as it is unable to predict diameter changes due to disruption.

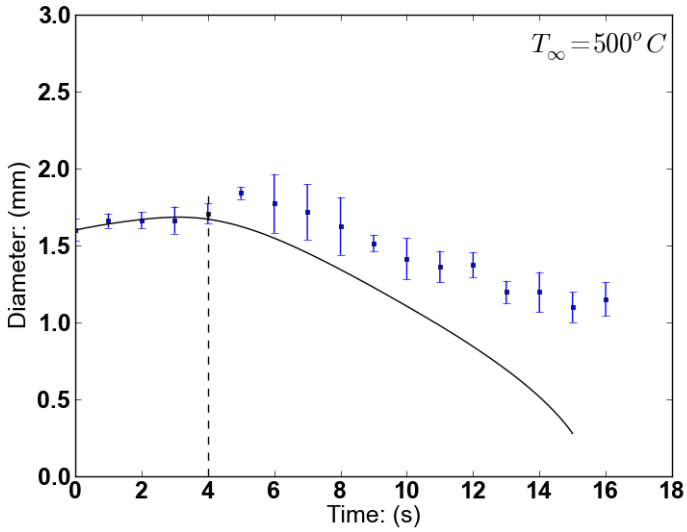

Figure 6.26: Comparison of measured droplet evaporation history and model prediction at 500°C. Solid line is calculated behavior. Experimental data are given as mean and standard deviation (error bars). Dashed line indicates onset of disruptions.

At this stage the size of the droplet enlarges past the point of thermal expansion, but afterwards the rate of droplet evaporation predicted is approximately the same as is seen in the experimental data. This continues until the droplet disappears leaving only a residue.

At 600°C (figure 6.27) similar results were observed. The initial heating phase of the droplet was similar to that at 500°C. The droplet size was observed to remain almost constant for the first 3 seconds, after which rapid bubbling and thermal expansion were observed to take place. The size of the droplet then decreased at the rate predicted by the model.

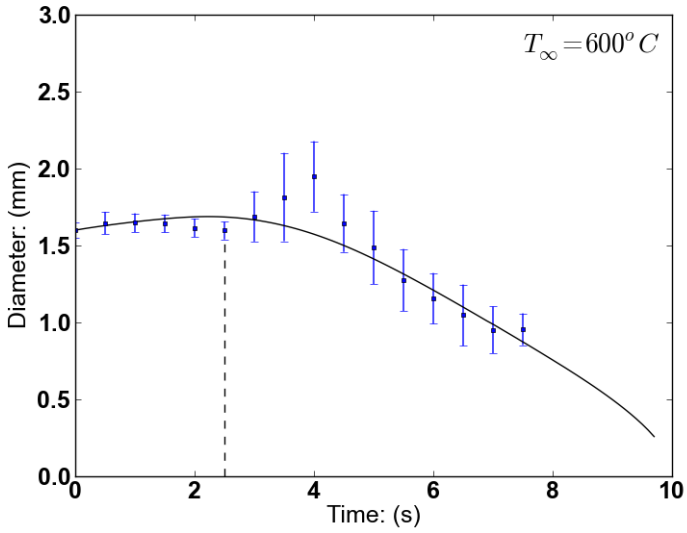

Figure 6.27: Comparison of measured droplet evaporation history and model prediction at 600°C. Solid line is calculated behavior. Experimental data are given as mean and standard deviation (error bars). Dashed line indicates onset of disruptions.

At 700°C (figure 6.28) a similar profile to the previous trials was observed, but the time until droplet disruption was only 2 seconds compared to 3 seconds at 600°C and the lifetime was approximately 6 seconds. After the expansion the slope of the droplet evaporation curve again closely matches that of the model.

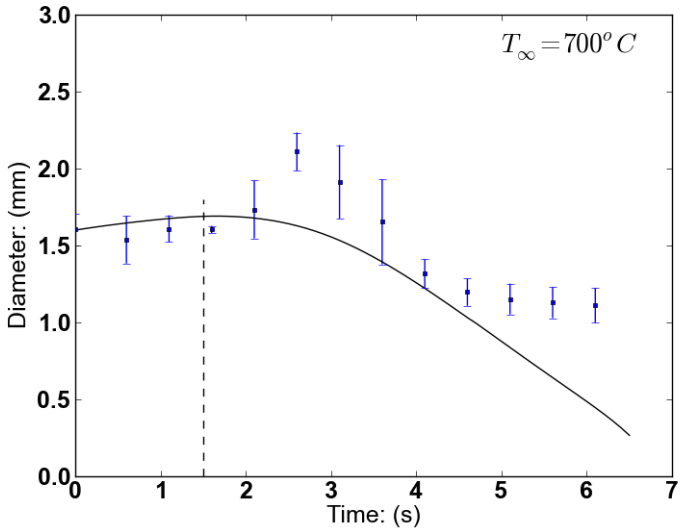

Figure 6.28: Comparison of measured droplet evaporation history and model prediction at 700°C. Solid line is calculated behavior. Experimental data are given as mean and standard deviation (error bars). Dashed line indicates onset of disruptions.

As the temperature increased the time until boiling and the droplet lifetime both decreased. At higher temperatures more disruptions were seen, especially at 700°C. In all the trials the numerical model was observed to closely approximate the profile except for the boiling behavior, once this ceased however a good agreement was again obtained.

At all three temperatures the calculated droplet size continues to drop near the end of the droplet history, whereas the experimental measurements level off at a value corresponding to the residue left after evaporation. In two cases, measured droplet sizes somewhat exceed the predicted values after disruption has occurred (Fig.6.26, 6.27). This may indicate that a residue is already forming in the remaining liquid owing to pyrolysis or polymerization; it also tends to confirm the earlier observation that significant quantities of mass were not ejected from the droplet during the disruption phase.

6.3 Comparison to a extended and simple model

The model used in this study was compared with an extended model using 8 distributions (table 5.4) and a simple model using 2 distributions (table 5.5). The temperature profile

predicted by the extended model (dotted line) very closely matches that of the standard model (solid line). The evaporation predictions of the extended model were slightly below that of the normal model however this deviation was slight.

The temperature profile of the simple model (dashed line) matches that of the standard model and extended model, the droplet lifetime predicted is smaller, about 2 sec. The droplet evaporation profile predicted by the simple model showed a significantly quicker rate of evaporation then the other two models. This could be due to the fact that only one chemical family (alkanes) was used.

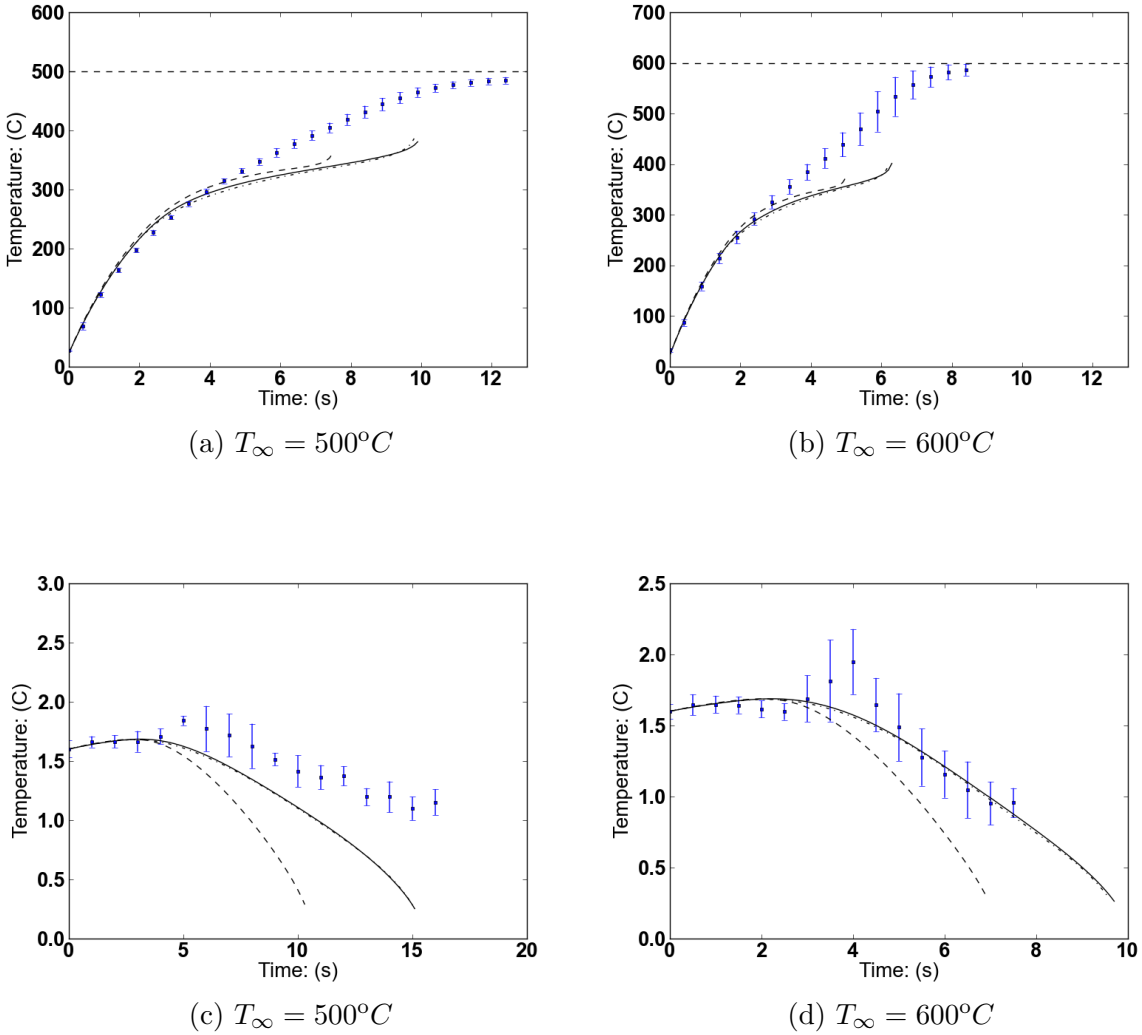

(a) $T_\infty = 500^oC$ (b) $T_\infty = 600^oC$

(c) $T_\infty = 500^oC$ (d) $T_\infty = 600^oC$

Figure 6.29: Comparison between simple, standard and extended models for droplet temperature profiles and evaporation. The standard model is denoted by a solid line, the extended model is denoted by a dotted line and the simple model by a dashed line.

For the standard and extended model presented here no adjustments were required to achieve a fit to the experimental results. The composition determined directly from the chemical analysis was sufficient. In the case of the simple model, since it considers only one chemical group, the values for this group could be modified to be representative of the fuel as a whole.

7 Conclusions

Raw chicken litter was converted in a thermal process to bio-oil, a dark thick black liquid with an appearance which resembled crude oil. This was then upgraded into a higher quality fuel through a series of physical and chemical processes. The resulting product resembled a hydrocarbon-based fuel, consisting largely of hydrocarbons (long chain n-alkanes, alkenes and alkyl-benzenes) along with long chain n-diols and fatty acids. Droplet evaporation testing and temperature tests were performed on the fuel at various furnace temperatures and the results compared to that of a numerical model which uses the principles of continuous thermodynamics to describe the fuel composition.

A comparison between the results of the droplet temperature experiments and the numerical model showed good agreement, indicating that the fuel composition as modeled by continuous thermodynamics gives a fairly accurate picture of the evaporation characteristics of the fuel. Droplet evaporation trials conducted on the fuel showed results consistent with theory: an initial liquid heating phase is followed by evaporation and distillation of the mixture with rising temperatures. The droplet then shrinks until it disappears. Droplet diameters predicted by the numerical model generally showed good agreement to those measured from droplet evaporation experiments, except as noted in the next paragraph.

Some deviations from the numerical model were observed. A fairly vigorous disruption of the droplet was observed at environmental temperatures above about 400°C, indicating internal bubbling and occasional micro-explosions. These were attributed to the internal boiling of lighter compounds within the droplet and have been seen mostly in other fuels with wide component boiling ranges. The result of this was rapid movement and enlarging and collapsing of the droplet as it underwent evaporation. An alternative explanation is the evolution of gas from pyrolysis of high boiling residual components of the fuel. These behaviours are complex and the ability to model them is beyond the scope of this thesis. Because the suspected mass loss is small, there should be little effect on the evaporation

history of the droplet.

Droplet temperature measurements allowed us to check the modeled composition of the fuel and show that the properties derived for it were reasonable. It was noted that temperatures measured in high temperature droplet temperature tests were found to deviate towards the end of the droplet lifetime, indicating either that the thermocouple had become exposed to the surroundings by disappearance of the liquid, or that solid residue was simply heating up as opposed to evaporating. The droplet fluctuations and movement were thought to increase this effect by contributing to exposing the thermocouple bead.

In all of the trials a solid residue was observed to form on the fibre bead and thermocouple. This was caused by the pyrolysis of heavier compounds within the fuel. The amount of residue observed was small. After each experiment the residue was removed by placing the bead in the flame from a candle.

The observed droplet lifetimes from the temperature measurements were mostly underpredicted by the model; this under prediction was attributed to pyrolysis within the droplet and the formation of a solid residue, which was not accounted for by the model. Because of the formation of residue it was difficult to determine the exact point at which the droplet had fully evaporated.

Overall, it can be concluded that the numerical model shown here gives predictions of droplet behavior of sufficient accuracy to be useful for models of the combustion of this fuel. No adjustments to the parameters of the model were required to achieve a fit to the data, these parameters were determined from the fuel composition alone.

To improve the predictions, further investigation into the formation of the solid residue could be examined as was done by Hallett and Clark (2006). By understanding the formation of the residue one could modify the model to account for this and improve the accuracy of the predictions.

References

D. Chiaramonti. Development of emulusions from biomass pyrolysis liquid and diesel and their use in engines - part 1: emulsion production. *Biomass and Bioenergy*, 25, 2003.

G.F. Chou and J.M. Prausnitz. Adiabatic flash calculations for continuous or simicontinuous mixtures using an equation of state. *Fluid Phase Equilibria*, 30, 1986.

P.C. Le Clercq and J. Bellan. Modeling of multicomponent-fuel drop-laden mixing layers having a multitude of species. *Proceedings of the Combustion Institute*, 30, 2005.

R.L. Cotterman and J.M. Prausnltz. Flash calculations for continuous or semicontrinuous mixtures using an equation of state. *Eng. Chem. Process Des. Dev.*, 24(2), 1985.

S. Czernik and A.V. Bridgwater. Overview of applications of biomass fast pyrolysis oil. *Energy and Fuels*, 18, 2004.

M. Garcia-Perez, A. Chaala, H. Pakdel, and D. Kretschmer. Characterization of bio-oils in chemical families. *Biomass and Bioenergy*, 31, 2007.

W.L.H. Hallett. A simple model for the vaporization of droplets with large numbers of components. *Combustion and Flame*, 121:334–344, 2000.

W.L.H. Hallett. Further notes on chicken manure bio-oil analysis. 2013.

W.L.H Hallett and Beauchamp-Kiss. Evaporation of single droplets of ethanolfuel oil mixtures. *Fuel*, 89, 2010.

W.L.H. Hallett and N.A. Clark. A model for the evaporation of biomass pyrolysis oil droplets. *Fuel*, 85, 2006.

M. Ikura, M. Stanciulescu, and E. Hogan. Emulsification of pyrolysis derived bio-oil in diesel fuel. *Biomass and Bioenergy*, 24, 2003.

G.L. Juste and JJ.S. Monfort. Preliminary test on combustion of wood derived fast pyrolysis oils in a gas turbine combustor. *Biomass and Bioenergy*, 19, 2000.

Z. Kazi, M. Schnitzer, C.M. Monreal, and P. Mayer. Separation and identification of heterocyclic nitrogen compounds in biooil derived by fast pyrolysis of chicken manure. *Journal of Environmental Science and Health Part B*, 46, 2011.

C.K. Law. *Combustion Physics*. Cambridge University Press, 1 edition, 2006.

A.M. Lippert and R.D. Reitz. Modeling of multicomponent fuels using continuous distributions with appliction to droplet evaporation and sprays. Technical report, Society of Automative Engineers, 1997.

R. Maggi and B. Delmon. Characterization and upgrading of bio-oils produced by rapid thermal processing. *Biomass and Bioenergy*, 7, 1994.

C.M. Monreal. Private Communication, 2009.

C.M. Monreal and G. Jandl. Private Communication, 2012.

A. Oasmaa and S. Czernik. Fuel oil quality of biomass pyrolysis oils - state of the art for the end users. *Energy and Fuels*, 13, 1999.

L.S. Ott, B.L. Smith, and T.J. Bruno. Advanced distillation curve measurement: Application to a bio-derived crude oil prepared from swine manure. *Fuel*, 87, 2008.

E. Pokorna, N. Postelmans, P. Jenicek, S. Schreurs, R. Carleer, and J. Yperman. Study of bio-oil and solids from flash pyrolysis of sewage sludges. *Fuel*, 88, 2009.

B.E. Poling, J.M. Prausnitz, and J.P. OConnell. *The Properties of Gases and Liquids*. McGraw-Hill, 5 edition, 2001.

Y. Ra and R.D. Reitz. The application of a multicomponent droplet vaporization model to gasoline direct injection engines. *Int. J. Engine Res*, 4(3), 2003.

M.I. Schnitzer, C.M. Monreal, G.A. Facey, and P.B. Fransham. The conversion of chicken manure to biooil by fast pyrolysis i. analysis of chicken manure, biooil and char by 13c

and 1h nmr and ftir spectrometry. *Journal of Environmental Sciences and Health Part B*, 42, 2007a.

M.I. Schnitzer, C.M. Monreal, and G. Jandl. The conversion of chicken manure to biooil by fast pyrolysis iii. analysis of chicken manure, biooil and char by py-fims and py-fdms. *Journal of Environmental Sciences and Health Part B*, 43, 2007b.

B. Scholze and D. Meier. Characterization of the water-insoluble fraction from pyrolysis oil (pyrolytic lignin). part i. py-gc/ms, ftir, and functional groups. *Journal of Analytical and Applied Pyrolysis*, 60, 2001.

C.R. Shaddix and D.R. Hardesty. Combustion properties of biomass flash pyrolysis oils: Final project report. Technical report, Sandia National Laboratories, Albuquerque, New Mexico 87185 and Livermore California 94550, April 1999.

A. Shihadeh and S. Hochgrebl. Impact of biomass pyrolysis oil process condition on ignition delay in compression ignition engines. *Energy and Fuels*, 16, 2002.

S. Tamim and W.L.H. Hallett. A continuous thermodynamic model for multicomponent droplet vaporization. *Chemical Engineering Science*, 18, 1995.

N. Whitely, R. Ozao, Y. Cao, and W. Pan. Multi-utilization of chicken litter as a biomass source. part i. combustion. *Energy and Fuels*, 20, 2006.

B.T. Willman and A.S. Teja. Continous thermodynamics of phase equilibria using a multivariate distribution function and an equation of state. *AIChE*, 32(12), 1986.

J. Yanik, C. Kornmayer, M. Saglam, and M. Yuksel. Fast pyrolysis of agricultural wastes: Characterization of pyrolysis products. *Fuel Processing Technology*, 88, 2007.

L. Zhang and S. Kong. Multicomponent vaporization modeling of bio-oil and its mixtures with other fuels. *Fuel*, 95, 2012.

A Estimated Property Values

A.1 Paraffins

MW: (g/mol)	Tb: (K)	Tc: (K)	Pc: (Bar)	hfg: (J/mol)	$(Tc - Tb)^{0.38}$
226.4	549.2	716.5	13.4	5.12e+07	7.0
240.5	561.6	728.2	12.6	5.34e+07	7.0
254.5	573.4	739.3	11.8	5.57e+07	7.0
268.5	584.5	749.6	11.1	5.79e+07	7.0
282.6	595.0	759.4	10.5	6.01e+07	7.0
296.6	605.0	768.8	9.9	6.23e+07	6.9
310.6	614.5	777.6	9.4	6.46e+07	6.9
324.6	623.6	786.0	9.0	6.68e+07	6.9
338.7	632.4	794.1	8.5	6.90e+07	6.9
352.7	640.7	801.8	8.2	7.12e+07	6.9
366.7	648.8	809.2	7.8	7.35e+07	6.9
380.7	656.5	816.4	7.5	7.57e+07	6.9
394.8	664.0	823.2	7.2	7.79e+07	6.9
408.8	671.1	829.8	6.9	8.01e+07	6.9
422.8	678.1	836.2	6.6	8.24e+07	6.8
436.9	684.8	842.3	6.4	8.46e+07	6.8
450.9	691.3	848.3	6.1	8.68e+07	6.8

Boiling and Critical Points (Sections 5.7.1, 5.7.2 & 5.7.3)

MW: (g/mol)	273 K	323 K	373 K
226.4	470.0	510.2	558.0
240.5	499.1	541.8	592.6
254.5	528.2	573.4	627.1
268.5	557.3	605.0	661.7
282.6	586.5	636.6	696.2
296.6	615.6	668.2	730.8
310.6	644.7	699.8	765.4
324.6	673.8	731.4	799.9
338.7	702.9	763.0	834.5
352.7	732.0	794.6	869.1
366.7	761.1	826.2	903.6
380.7	790.3	857.8	938.2
394.8	819.4	889.4	972.8
408.8	848.5	921.0	1007.3
422.8	877.6	952.6	1041.9
436.9	906.7	984.2	1076.5
450.9	935.8	1015.8	1111.0

Liquid Specific Heat: (kJ/kmolK) (Section 5.7.4)

MW: (g/mol)	400 K	700 K	1000 K
226.4	473.9	701.7	844.8
240.5	503.0	744.7	896.4
254.5	532.2	787.7	948.0
268.5	561.3	830.7	999.6
282.6	590.5	873.7	1051.1
296.6	619.6	916.7	1102.7
310.6	648.8	959.8	1154.3
324.6	677.9	1002.8	1205.9
338.7	707.1	1045.8	1257.5
352.7	736.2	1088.8	1309.1
366.7	765.4	1131.8	1360.7
380.7	794.5	1174.8	1412.3
394.8	823.7	1217.9	1463.9
408.8	852.8	1260.9	1515.5
422.8	882.0	1303.9	1567.1
436.9	911.1	1346.9	1618.6
450.9	940.3	1389.9	1670.2

Vapour Specific Heat: (kJ/kmolK) (Section 5.7.5)

MW: (g/mol)	293 K	383 K	503 K
226.4	0.293	0.316	0.347
240.5	0.309	0.334	0.366
254.5	0.326	0.351	0.386
268.5	0.342	0.369	0.405
282.6	0.358	0.387	0.424
296.6	0.375	0.404	0.444
310.6	0.391	0.422	0.463
324.6	0.407	0.439	0.482
338.7	0.423	0.457	0.502
352.7	0.440	0.475	0.521
366.7	0.456	0.492	0.540
380.7	0.472	0.510	0.560
394.8	0.489	0.527	0.579
408.8	0.505	0.545	0.598
422.8	0.521	0.563	0.618
436.9	0.538	0.580	0.637
450.9	0.554	0.598	0.656

Liquid Specific Volume: (cm^3/mol) (Section 5.7.8)

MW: (g/mol)	400 K	700 K	1000 K
226.4	1.57e-02	4.30e-02	7.02e-02
240.5	1.55e-02	4.25e-02	6.94e-02
254.5	1.53e-02	4.20e-02	6.87e-02
268.5	1.52e-02	4.16e-02	6.80e-02
282.6	1.50e-02	4.11e-02	6.72e-02
296.6	1.48e-02	4.06e-02	6.65e-02
310.6	1.46e-02	4.02e-02	6.57e-02
324.6	1.44e-02	3.97e-02	6.50e-02
338.7	1.42e-02	3.92e-02	6.43e-02
352.7	1.40e-02	3.88e-02	6.35e-02
366.7	1.38e-02	3.83e-02	6.28e-02
380.7	1.37e-02	3.78e-02	6.20e-02
394.8	1.35e-02	3.74e-02	6.13e-02
408.8	1.33e-02	3.69e-02	6.06e-02
422.8	1.31e-02	3.65e-02	5.98e-02
436.9	1.29e-02	3.60e-02	5.91e-02
450.9	1.27e-02	3.55e-02	5.83e-02

Vapour Thermal Conductivity: (W/mK) (Section 5.7.7)

MW: (g/mol)	400 K	700 K	1000 K
226.4	8.19e-06	2.23e-05	4.13e-05
240.5	7.93e-06	2.16e-05	4.00e-05
254.5	7.69e-06	2.10e-05	3.89e-05
268.5	7.47e-06	2.04e-05	3.78e-05
282.6	7.26e-06	1.99e-05	3.68e-05
296.6	7.08e-06	1.94e-05	3.59e-05
310.6	6.90e-06	1.89e-05	3.50e-05
324.6	6.74e-06	1.85e-05	3.42e-05
338.7	6.59e-06	1.81e-05	3.35e-05
352.7	6.44e-06	1.77e-05	3.28e-05
366.7	6.31e-06	1.73e-05	3.21e-05
380.7	6.18e-06	1.70e-05	3.15e-05
394.8	6.06e-06	1.67e-05	3.09e-05
408.8	5.95e-06	1.64e-05	3.03e-05
422.8	5.84e-06	1.61e-05	2.98e-05
436.9	5.74e-06	1.58e-05	2.93e-05
450.9	5.64e-06	1.55e-05	2.88e-05

Vapour Diffusion: (m^2/s) (Section 5.7.6)

a_C:	593.9
b_C:	0.579
a_B:	416.3
b_B:	0.625

Boiling and Critical Point Coefficients (Sections: 5.7.1 & 5.7.2) (Equations: 5.8 & 5.11)

a_V:	2.60e-02
b_V:	3.98e-03
a_P:	19.6
b_P:	-3.12e-02

Critical Volume and Pressure Coefficients (Section: 5.7.1) (Equations: 5.9)

a_L:	1.53e+07
b_L:	1.59e+05

Enthalpy of Vaporization Coefficients (Section: 5.7.3) (Equations: 5.13)

a_L:	1.70e+00
b_L:	-4.70e-04
b_L:	6.74e-06

Liquid Specific Heat Coefficients (Section: 5.7.4) (Equation: 5.19)

a_1:	3.63e-01	b_1:	-7.79e-03
a_2:	-1.18e-03	b_2:	8.15e-04
a_3:	3.80e-06	b_3:	-4.66e-07
a_4:	-1.55e-09	b_4:	1.02e-10

Vapour Specific Heat Coefficients (Section: 5.7.5) (Equations: 5.25, 5.26 & 5.27)

a_D:	2.05e-09
b_D:	-2.14e-12
b_Φ:	230.0

Diffusion Coefficients (Section: 5.7.6) (Equation: 5.37)

a_D:	2.97e-02
b_D:	1.16e-03
α_P:	8.80e-04

Liquid Specific Volume Coefficients (Section: 5.7.8) (Equation: 5.48)

a_{KC}:	-2.35e-02
b_{KT}:	1.06e-04
b_{KC}:	1.29e-05
b_{KT}:	-6.58e-08

Thermal Conductivity Coefficients (Section: 5.7.7) (Equation: 5.45, 5.46 & 5.47)

A.2 Alkenes

MW: (g/mol)	Tb: (K)	Tc: (K)	Pc: (Bar)	hfg: (J/mol)	$(Tc - Tb)^{0.38}$
224.4	548.8	716.0	13.9	5.05e+07	7.0
238.5	561.3	727.7	13.0	5.28e+07	7.0
252.5	573.0	738.8	12.2	5.50e+07	7.0
266.5	584.1	749.2	11.5	5.72e+07	7.0
280.5	594.7	759.0	10.8	5.94e+07	7.0
294.6	604.7	768.3	10.2	6.17e+07	6.9
308.6	614.2	777.2	9.7	6.39e+07	6.9
322.6	623.4	785.7	9.2	6.61e+07	6.9
336.6	632.1	793.8	8.8	6.83e+07	6.9
350.7	640.5	801.5	8.4	7.06e+07	6.9
364.7	648.5	808.9	8.0	7.28e+07	6.9
378.7	656.3	816.0	7.6	7.50e+07	6.9
392.8	663.7	822.9	7.3	7.73e+07	6.9
406.8	670.9	829.5	7.0	7.95e+07	6.9
420.8	677.9	835.9	6.7	8.17e+07	6.8
434.8	684.6	842.0	6.5	8.39e+07	6.8
448.9	691.1	848.0	6.3	8.62e+07	6.8

Boiling and Critical Points (Sections 5.7.1, 5.7.2 & 5.7.3)

MW: (g/mol)	273 K	323 K	373 K
224.4	460.4	497.3	541.9
238.5	489.1	528.4	575.8
252.5	517.9	559.5	609.6
266.5	546.7	590.6	643.5
280.5	575.5	621.6	677.4
294.6	604.2	652.7	711.2
308.6	633.0	683.8	745.1
322.6	661.8	714.9	779.0
336.6	690.6	746.0	812.9
350.7	719.3	777.1	846.7
364.7	748.1	808.1	880.6
378.7	776.9	839.2	914.5
392.8	805.6	870.3	948.3
406.8	834.4	901.4	982.2
420.8	863.2	932.5	1016.1
434.8	892.0	963.5	1049.9
448.9	920.7	994.6	1083.8

Liquid Specific Heat: (kJ/kmolK) (Section 5.7.4)

MW: (g/mol)	400 K	700 K	1000 K
224.4	460.3	679.4	816.3
238.5	489.5	722.4	867.9
252.5	518.6	765.4	919.5
266.5	547.8	808.5	971.0
280.5	576.9	851.5	1022.6
294.6	606.1	894.5	1074.2
308.6	635.2	937.5	1125.8
322.6	664.4	980.5	1177.4
336.6	693.5	1023.5	1229.0
350.7	722.7	1066.6	1280.6
364.7	751.8	1109.6	1332.2
378.7	781.0	1152.6	1383.8
392.8	810.1	1195.6	1435.4
406.8	839.3	1238.6	1487.0
420.8	868.4	1281.6	1538.5
434.8	897.6	1324.7	1590.1
448.9	926.7	1367.7	1641.7

Vapour Specific Heat: (kJ/kmolK) (Section 5.7.5)

MW: (g/mol)	293 K	383 K	503 K
224.4	0.288	0.311	0.342
238.5	0.304	0.329	0.361
252.5	0.321	0.346	0.381
266.5	0.337	0.364	0.400
280.5	0.353	0.382	0.419
294.6	0.370	0.399	0.439
308.6	0.386	0.417	0.458
322.6	0.402	0.434	0.477
336.6	0.418	0.452	0.497
350.7	0.435	0.470	0.516
364.7	0.451	0.487	0.535
378.7	0.467	0.505	0.555
392.8	0.484	0.522	0.574
406.8	0.500	0.540	0.593
420.8	0.516	0.558	0.613
434.8	0.533	0.575	0.632
448.9	0.549	0.593	0.652

Liquid Specific Volume: (cm^3/mol) (Section 5.7.8)

MW: (g/mol)	400 K	700 K	1000 K
224.4	1.55e-02	4.23e-02	6.90e-02
238.5	1.54e-02	4.18e-02	6.83e-02
252.5	1.52e-02	4.14e-02	6.76e-02
266.5	1.50e-02	4.09e-02	6.69e-02
280.5	1.48e-02	4.05e-02	6.62e-02
294.6	1.46e-02	4.01e-02	6.55e-02
308.6	1.45e-02	3.96e-02	6.48e-02
322.6	1.43e-02	3.92e-02	6.41e-02
336.6	1.41e-02	3.88e-02	6.34e-02
350.7	1.39e-02	3.83e-02	6.27e-02
364.7	1.37e-02	3.79e-02	6.20e-02
378.7	1.36e-02	3.74e-02	6.13e-02
392.8	1.34e-02	3.70e-02	6.06e-02
406.8	1.32e-02	3.66e-02	5.99e-02
420.8	1.30e-02	3.61e-02	5.92e-02
434.8	1.28e-02	3.57e-02	5.85e-02
448.9	1.27e-02	3.53e-02	5.78e-02

Vapour Thermal Conductivity: (W/mK) (Section 5.7.7)

MW: (g/mol)	400 K	700 K	1000 K
224.4	8.25e-06	2.25e-05	4.16e-05
238.5	7.98e-06	2.18e-05	4.03e-05
252.5	7.74e-06	2.11e-05	3.91e-05
266.5	7.52e-06	2.06e-05	3.81e-05
280.5	7.31e-06	2.00e-05	3.70e-05
294.6	7.12e-06	1.95e-05	3.61e-05
308.6	6.94e-06	1.90e-05	3.52e-05
322.6	6.78e-06	1.86e-05	3.44e-05
336.6	6.62e-06	1.82e-05	3.37e-05
350.7	6.48e-06	1.78e-05	3.30e-05
364.7	6.34e-06	1.74e-05	3.23e-05
378.7	6.21e-06	1.71e-05	3.16e-05
392.8	6.09e-06	1.67e-05	3.10e-05
406.8	5.97e-06	1.64e-05	3.05e-05
420.8	5.86e-06	1.61e-05	2.99e-05
434.8	5.76e-06	1.59e-05	2.94e-05
448.9	5.66e-06	1.56e-05	2.89e-05

Vapour Diffusion: (m^2/s) (Section 5.7.6)

a_C:	594.2
b_C:	0.580
a_B:	416.9
b_B:	0.626

Boiling and Critical Point Coefficients (Sections: 5.7.1 & 5.7.2) (Equations: 5.8 & 5.11)

a_V:	1.98e-02
b_V:	3.98e-03
a_P:	20.2
b_P:	-3.27e-02

Critical Volume and Pressure Coefficients (Section: 5.7.1) (Equations: 5.9)

a_L:	1.49e+07
b_L:	1.59e+05

Enthalpy of Vaporization Coefficients (Section: 5.7.3) (Equations: 5.13)

a_L:	1.75e+00
b_L:	-7.70e-04
b_L:	6.82e-06

Liquid Specific Heat Coefficients (Section: 5.7.4) (Equation: 5.19)

a_1:	-1.24e-02	b_1:	-7.79e-03
a_2:	-1.95e-03	b_2:	8.15e-04
a_3:	1.08e-07	b_3:	-4.66e-07
a_4:	7.46e-10	b_4:	1.02e-10

Vapour Specific Heat Coefficients (Section: 5.7.5) (Equations: 5.25, 5.26 & 5.27)

a_D:	2.06e-09
b_D:	-2.17e-12
b_Φ:	230.0

Diffusion Coefficients (Section: 5.7.6) (Equation: 5.37)

a_D:	2.70e-02
b_D:	1.16e-03
α_P:	8.90e-04

Liquid Specific Volume Coefficients (Section: 5.7.8) (Equation: 5.48)

a_{KC}:	-2.27e-02
b_{KT}:	1.03e-04
b_{KC}:	1.16e-05
b_{KT}:	-6.12e-08

Thermal Conductivity Coefficients (Section: 5.7.7) (Equation: 5.45, 5.46 & 5.47)

A.3 Alkyl-benzenes

MW: (g/mol)	Tb: (K)	Tc: (K)	Pc: (Bar)	hfg: (J/mol)	$(Tc - Tb)^{0.38}$
218.4	551.6	737.3	16.8	5.35e+07	7.3
232.4	563.9	747.8	15.6	5.57e+07	7.3
246.4	575.5	757.7	14.5	5.79e+07	7.2
260.5	586.5	767.1	13.6	6.02e+07	7.2
274.5	596.9	776.1	12.7	6.24e+07	7.2
288.5	606.8	784.6	11.9	6.46e+07	7.2
302.5	616.3	792.7	11.2	6.68e+07	7.1
316.6	625.3	800.5	10.6	6.91e+07	7.1
330.6	634.0	807.9	10.1	7.13e+07	7.1
344.6	642.3	815.1	9.5	7.35e+07	7.1
358.7	650.2	822.0	9.1	7.57e+07	7.1
372.7	657.9	828.6	8.6	7.80e+07	7.1
386.7	665.3	835.0	8.2	8.02e+07	7.0
400.7	672.5	841.2	7.9	8.24e+07	7.0
414.8	679.4	847.2	7.5	8.46e+07	7.0
428.8	686.0	853.0	7.2	8.69e+07	7.0
442.8	692.5	858.6	6.9	8.91e+07	7.0

Boiling and Critical Points (Sections 5.7.1, 5.7.2 & 5.7.3)

MW: (g/mol)	273 K	323 K	373 K
218.4	417.7	453.8	496.9
232.4	444.5	482.9	528.8
246.4	471.3	512.1	560.7
260.5	498.2	541.2	592.6
274.5	525.0	570.3	624.5
288.5	551.8	599.5	656.4
302.5	578.6	628.6	688.3
316.6	605.5	657.8	720.2
330.6	632.3	686.9	752.2
344.6	659.1	716.1	784.1
358.7	686.0	745.2	816.0
372.7	712.8	774.4	847.9
386.7	739.6	803.5	879.8
400.7	766.4	832.6	911.7
414.8	793.3	861.8	943.6
428.8	820.1	890.9	975.5
442.8	846.9	920.1	1007.5

Liquid Specific Heat: (kJ/kmolK) (Section 5.7.4)

MW: (g/mol)	400 K	700 K	1000 K
218.4	401.8	594.1	713.3
232.4	430.9	637.1	764.9
246.4	460.1	680.1	816.5
260.5	489.2	723.2	868.1
274.5	518.3	766.2	919.7
288.5	547.5	809.2	971.3
302.5	576.6	852.2	1022.9
316.6	605.8	895.2	1074.5
330.6	634.9	938.2	1126.1
344.6	664.1	981.3	1177.6
358.7	693.2	1024.3	1229.2
372.7	722.4	1067.3	1280.8
386.7	751.5	1110.3	1332.4
400.7	780.7	1153.3	1384.0
414.8	809.8	1196.3	1435.6
428.8	839.0	1239.4	1487.2
442.8	868.1	1282.4	1538.8

Vapour Specific Heat: (kJ/kmolK) (Section 5.7.5)

MW: (g/mol)	293 K	453 K	573 K
218.4	0.254	0.278	0.295
232.4	0.271	0.295	0.314
246.4	0.287	0.313	0.333
260.5	0.303	0.331	0.352
274.5	0.320	0.349	0.371
288.5	0.336	0.367	0.390
302.5	0.352	0.384	0.408
316.6	0.369	0.402	0.427
330.6	0.385	0.420	0.446
344.6	0.401	0.438	0.465
358.7	0.417	0.456	0.484
372.7	0.434	0.473	0.503
386.7	0.450	0.491	0.522
400.7	0.466	0.509	0.541
414.8	0.483	0.527	0.560
428.8	0.499	0.545	0.579
442.8	0.515	0.562	0.598

Liquid Specific Volume: (cm^3/mol) (Section 5.7.8)

MW: (g/mol)	400 K	700 K	1000 K
218.4	1.45e-02	3.97e-02	6.48e-02
232.4	1.44e-02	3.93e-02	6.43e-02
246.4	1.43e-02	3.90e-02	6.38e-02
260.5	1.41e-02	3.87e-02	6.32e-02
274.5	1.40e-02	3.83e-02	6.27e-02
288.5	1.38e-02	3.80e-02	6.22e-02
302.5	1.37e-02	3.77e-02	6.16e-02
316.6	1.36e-02	3.73e-02	6.11e-02
330.6	1.34e-02	3.70e-02	6.06e-02
344.6	1.33e-02	3.67e-02	6.00e-02
358.7	1.31e-02	3.63e-02	5.95e-02
372.7	1.30e-02	3.60e-02	5.90e-02
386.7	1.29e-02	3.57e-02	5.84e-02
400.7	1.27e-02	3.53e-02	5.79e-02
414.8	1.26e-02	3.50e-02	5.74e-02
428.8	1.24e-02	3.46e-02	5.68e-02
442.8	1.23e-02	3.43e-02	5.63e-02

Vapour Thermal Conductivity: (W/mK) (Section 5.7.7)

MW: (g/mol)	400 K	700 K	1000 K
218.4	8.58e-06	2.34e-05	4.34e-05
232.4	8.29e-06	2.27e-05	4.19e-05
246.4	8.02e-06	2.19e-05	4.06e-05
260.5	7.77e-06	2.13e-05	3.94e-05
274.5	7.55e-06	2.07e-05	3.83e-05
288.5	7.34e-06	2.01e-05	3.73e-05
302.5	7.15e-06	1.96e-05	3.63e-05
316.6	6.97e-06	1.91e-05	3.55e-05
330.6	6.80e-06	1.87e-05	3.46e-05
344.6	6.65e-06	1.83e-05	3.39e-05
358.7	6.50e-06	1.79e-05	3.31e-05
372.7	6.36e-06	1.75e-05	3.25e-05
386.7	6.23e-06	1.71e-05	3.18e-05
400.7	6.11e-06	1.68e-05	3.12e-05
414.8	6.00e-06	1.65e-05	3.06e-05
428.8	5.89e-06	1.62e-05	3.01e-05
442.8	5.78e-06	1.59e-05	2.96e-05

Vapour Diffusion: (m^2/s) (Section 5.7.6)

a_C:	627.8
b_C:	0.534
a_B:	424.6
b_B:	0.620

Boiling and Critical Point Coefficients (Sections: 5.7.1 & 5.7.2) (Equations: 5.8 & 5.11)

a_V:	-3.97e-02
b_V:	3.98e-03
a_P:	24.6
b_P:	-4.22e-02

Critical Volume and Pressure Coefficients (Section: 5.7.1) (Equations: 5.9)

a_L:	1.88e+07
b_L:	1.59e+05

Enthalpy of Vaporization Coefficients (Section: 5.7.3) (Equations: 5.13)

a_L:	1.58e+00
b_L:	-5.20e-04
b_L:	6.42e-06

Liquid Specific Heat Coefficients (Section: 5.7.4) (Equation: 5.19)

a_1:	-3.78e+00	b_1:	-7.79e-03
a_2:	-4.10e-03	b_2:	8.15e-04
a_3:	-3.71e-06	b_3:	-4.66e-07
a_4:	2.34e-09	b_4:	1.02e-10

Vapour Specific Heat Coefficients (Section: 5.7.5) (Equations: 5.25, 5.26 & 5.27)

a_D:	2.11e-09
b_D:	-2.31e-12
b_Φ:	216.0

Diffusion Coefficients (Section: 5.7.6) (Equation: 5.37)

a_D:	3.97e-04
b_D:	1.16e-03
α_P:	5.70e-04

Liquid Specific Volume Coefficients (Section: 5.7.8) (Equation: 5.48)

a_{KC}:	-2.09e-02
b_{KT}:	9.40e-05
b_{KC}:	8.71e-06
b_{KT}:	-4.67e-08

Thermal Conductivity Coefficients (Section: 5.7.7) (Equation: 5.45, 5.46 & 5.47)

A.4 Fatty Acids

MW: (g/mol)	Tb: (K)	Tc: (K)	Pc: (Bar)	hfg: (J/mol)	$(Tc - Tb)^{0.38}$
256.4	608.5	780.4	14.1	6.84e+07	7.1
270.5	617.9	788.7	13.2	7.06e+07	7.1
284.5	626.8	796.6	12.4	7.28e+07	7.0
298.5	635.4	804.3	11.7	7.51e+07	7.0
312.5	643.7	811.6	11.0	7.73e+07	7.0
326.6	651.6	818.6	10.4	7.95e+07	7.0
340.6	659.2	825.4	9.8	8.17e+07	7.0
354.6	666.6	831.9	9.3	8.40e+07	7.0
368.6	673.7	838.2	8.9	8.62e+07	7.0
382.7	680.5	844.3	8.5	8.84e+07	6.9
396.7	687.2	850.1	8.1	9.06e+07	6.9
410.7	693.6	855.8	7.7	9.29e+07	6.9
424.8	699.8	861.4	7.4	9.51e+07	6.9
438.8	705.9	866.7	7.1	9.73e+07	6.9
452.8	711.8	871.9	6.8	9.95e+07	6.9
466.8	717.5	877.0	6.6	1.02e+08	6.9
480.9	723.0	881.9	6.3	1.04e+08	6.9

Boiling and Critical Points (Sections 5.7.1, 5.7.2 & 5.7.3)

MW: (g/mol)	273 K	323 K	373 K
256.4	518.2	563.9	617.5
270.5	546.6	594.8	651.3
284.5	574.9	625.6	685.1
298.5	603.3	656.4	718.9
312.5	631.6	687.3	752.7
326.6	660.0	718.1	786.4
340.6	688.3	749.0	820.2
354.6	716.7	779.8	854.0
368.6	745.0	810.7	887.8
382.7	773.4	841.5	921.6
396.7	801.7	872.4	955.4
410.7	830.1	903.2	989.1
424.8	858.4	934.1	1022.9
438.8	886.8	964.9	1056.7
452.8	915.1	995.7	1090.5
466.8	943.5	1026.6	1124.3
480.9	971.8	1057.4	1158.0

Liquid Specific Heat: (kJ/kmolK) (Section 5.7.4)

MW: (g/mol)	400 K	700 K	1000 K
256.4	485.7	704.0	842.6
270.5	514.8	747.0	894.2
284.5	544.0	790.0	945.8
298.5	573.1	833.0	997.4
312.5	602.3	876.0	1049.0
326.6	631.4	919.1	1100.6
340.6	660.6	962.1	1152.2
354.6	689.7	1005.1	1203.8
368.6	718.9	1048.1	1255.4
382.7	748.0	1091.1	1307.0
396.7	777.2	1134.1	1358.5
410.7	806.3	1177.2	1410.1
424.8	835.5	1220.2	1461.7
438.8	864.6	1263.2	1513.3
452.8	893.8	1306.2	1564.9
466.8	922.9	1349.2	1616.5
480.9	952.1	1392.2	1668.1

Vapour Specific Heat: (kJ/kmolK) (Section 5.7.5)

MW: (g/mol)	293 K	383 K	503 K
256.4	0.288	0.310	0.340
270.5	0.304	0.328	0.359
284.5	0.321	0.345	0.379
298.5	0.337	0.363	0.398
312.5	0.353	0.381	0.417
326.6	0.370	0.398	0.436
340.6	0.386	0.416	0.456
354.6	0.402	0.433	0.475
368.6	0.418	0.451	0.494
382.7	0.435	0.468	0.513
396.7	0.451	0.486	0.533
410.7	0.467	0.504	0.552
424.8	0.484	0.521	0.571
438.8	0.500	0.539	0.590
452.8	0.516	0.556	0.610
466.8	0.533	0.574	0.629
480.9	0.549	0.591	0.648

Liquid Specific Volume: (cm^3/mol) (Section 5.7.8)

MW: (g/mol)	400 K	700 K	1000 K
256.4	1.43e-02	3.85e-02	6.28e-02
270.5	1.41e-02	3.82e-02	6.24e-02
284.5	1.40e-02	3.79e-02	6.19e-02
298.5	1.39e-02	3.76e-02	6.14e-02
312.5	1.37e-02	3.73e-02	6.10e-02
326.6	1.36e-02	3.70e-02	6.05e-02
340.6	1.35e-02	3.67e-02	6.00e-02
354.6	1.33e-02	3.64e-02	5.95e-02
368.6	1.32e-02	3.61e-02	5.91e-02
382.7	1.31e-02	3.58e-02	5.86e-02
396.7	1.30e-02	3.55e-02	5.81e-02
410.7	1.28e-02	3.52e-02	5.76e-02
424.8	1.27e-02	3.49e-02	5.72e-02
438.8	1.26e-02	3.46e-02	5.67e-02
452.8	1.24e-02	3.43e-02	5.62e-02
466.8	1.23e-02	3.40e-02	5.57e-02
480.9	1.22e-02	3.37e-02	5.53e-02

Vapour Thermal Conductivity: (W/mK) (Section 5.7.7)

MW: (g/mol)	400 K	700 K	1000 K
256.4	7.91e-06	2.17e-05	4.02e-05
270.5	7.67e-06	2.10e-05	3.90e-05
284.5	7.46e-06	2.05e-05	3.79e-05
298.5	7.26e-06	1.99e-05	3.69e-05
312.5	7.07e-06	1.94e-05	3.60e-05
326.6	6.90e-06	1.90e-05	3.52e-05
340.6	6.74e-06	1.85e-05	3.44e-05
354.6	6.59e-06	1.81e-05	3.36e-05
368.6	6.44e-06	1.77e-05	3.29e-05
382.7	6.31e-06	1.74e-05	3.22e-05
396.7	6.18e-06	1.70e-05	3.16e-05
410.7	6.06e-06	1.67e-05	3.10e-05
424.8	5.95e-06	1.64e-05	3.04e-05
438.8	5.84e-06	1.61e-05	2.99e-05
452.8	5.74e-06	1.58e-05	2.94e-05
466.8	5.64e-06	1.56e-05	2.89e-05
480.9	5.55e-06	1.53e-05	2.84e-05

Vapour Diffusion: (m^2/s) (Section 5.7.6)

a_C:	670.2
b_C:	0.449
a_B:	484.2
b_B:	0.506

Boiling and Critical Point Coefficients (Sections: 5.7.1 & 5.7.2) (Equations: 5.8 & 5.11)

a_V:	-6.63e-02
b_V:	3.98e-03
a_P:	21.7
b_P:	-3.35e-02

Critical Volume and Pressure Coefficients (Section: 5.7.1) (Equations: 5.9)

a_L:	2.77e+07
b_L:	1.59e+05

Enthalpy of Vaporization Coefficients (Section: 5.7.3) (Equations: 5.13)

a_L:	1.60e+00
b_L:	-1.47e-04
b_L:	6.22e-06

Liquid Specific Heat Coefficients (Section: 5.7.4) (Equation: 5.19)

a_1:	1.15e+00	b_1:	-7.79e-03
a_2:	-1.95e-02	b_2:	8.15e-04
a_3:	9.06e-06	b_3:	-4.66e-07
a_4:	-1.24e-09	b_4:	1.02e-10

Vapour Specific Heat Coefficients (Section: 5.7.5) (Equations: 5.25, 5.26 & 5.27)

a_D:	2.04e-09
b_D:	-2.01e-12
b_Φ:	234.0

Diffusion Coefficients (Section: 5.7.6) (Equation: 5.37)

a_D:	-1.02e-02
b_D:	1.16e-03
α_P:	8.60e-04

Liquid Specific Volume Coefficients (Section: 5.7.8) (Equation: 5.48)

a_{KC}:	-1.99e-02
b_{KT}:	9.15e-05
b_{KC}:	7.04e-06
b_{KT}:	-4.08e-08

Thermal Conductivity Coefficients (Section: 5.7.7) (Equation: 5.45, 5.46 & 5.47)

A.5 Diols

MW: (g/mol)	Tb: (K)	Tc: (K)	Pc: (Bar)	hfg: (J/mol)	$(Tc - Tb)^{0.38}$
258.4	628.9	787.6	13.1	8.46e+07	6.9
272.5	635.6	793.8	12.7	8.68e+07	6.9
286.5	642.3	800.0	12.2	8.90e+07	6.8
300.5	649.0	806.3	11.7	9.12e+07	6.8
314.6	655.7	812.5	11.3	9.35e+07	6.8
328.6	662.4	818.7	10.8	9.57e+07	6.8
342.6	669.1	824.9	10.3	9.79e+07	6.8
356.6	675.8	831.2	9.8	1.00e+08	6.8
370.7	682.5	837.4	9.4	1.02e+08	6.8
384.7	689.2	843.6	8.9	1.05e+08	6.8
398.7	695.9	849.9	8.4	1.07e+08	6.8
412.7	702.6	856.1	8.0	1.09e+08	6.8
426.8	709.3	862.3	7.5	1.11e+08	6.8
440.8	716.0	868.5	7.0	1.14e+08	6.8
454.8	722.7	874.8	6.5	1.16e+08	6.7
468.9	729.4	881.0	6.1	1.18e+08	6.7
482.9	736.1	887.2	5.6	1.20e+08	6.7

Boiling and Critical Points (Sections 5.7.1, 5.7.2 & 5.7.3)

MW: (g/mol)	273 K	323 K	373 K
258.4	538.9	585.0	639.6
272.5	568.1	616.8	674.3
286.5	597.4	648.5	709.0
300.5	626.6	680.3	743.7
314.6	655.9	712.0	778.4
328.6	685.1	743.8	813.2
342.6	714.3	775.6	847.9
356.6	743.6	807.3	882.6
370.7	772.8	839.1	917.3
384.7	802.1	870.8	952.0
398.7	831.3	902.6	986.7
412.7	860.6	934.3	1021.4
426.8	889.8	966.1	1056.1
440.8	919.1	997.8	1090.9
454.8	948.3	1029.6	1125.6
468.9	977.6	1061.3	1160.3
482.9	1006.8	1093.1	1195.0

Liquid Specific Heat: (kJ/kmolK) (Section 5.7.4)

MW: (g/mol)	400 K	700 K	1000 K
258.4	499.9	724.9	869.2
272.5	529.0	767.9	920.8
286.5	558.2	810.9	972.4
300.5	587.3	853.9	1024.0
314.6	616.5	897.0	1075.6
328.6	645.6	940.0	1127.2
342.6	674.8	983.0	1178.7
356.6	703.9	1026.0	1230.3
370.7	733.1	1069.0	1281.9
384.7	762.2	1112.0	1333.5
398.7	791.4	1155.1	1385.1
412.7	820.5	1198.1	1436.7
426.8	849.7	1241.1	1488.3
440.8	878.8	1284.1	1539.9
454.8	908.0	1327.1	1591.5
468.9	937.1	1370.1	1643.1
482.9	966.3	1413.2	1694.7

Vapour Specific Heat: (kJ/kmolK) (Section 5.7.5)

MW: (g/mol)	293 K	383 K	503 K
258.4	0.282	0.308	0.342
272.5	0.299	0.326	0.362
286.5	0.315	0.343	0.381
300.5	0.331	0.361	0.401
314.6	0.348	0.379	0.421
328.6	0.364	0.397	0.440
342.6	0.380	0.415	0.460
356.6	0.397	0.432	0.480
370.7	0.413	0.450	0.500
384.7	0.429	0.468	0.519
398.7	0.446	0.486	0.539
412.7	0.462	0.503	0.559
426.8	0.478	0.521	0.579
440.8	0.495	0.539	0.598
454.8	0.511	0.557	0.618
468.9	0.527	0.575	0.638
482.9	0.543	0.592	0.658

Liquid Specific Volume: (cm^3/mol) (Section 5.7.8)

MW: (g/mol)	400 K	700 K	1000 K
258.4	1.44e-02	3.91e-02	6.38e-02
272.5	1.43e-02	3.88e-02	6.33e-02
286.5	1.41e-02	3.85e-02	6.28e-02
300.5	1.40e-02	3.82e-02	6.23e-02
314.6	1.39e-02	3.78e-02	6.18e-02
328.6	1.37e-02	3.75e-02	6.13e-02
342.6	1.36e-02	3.72e-02	6.08e-02
356.6	1.35e-02	3.69e-02	6.03e-02
370.7	1.33e-02	3.65e-02	5.97e-02
384.7	1.32e-02	3.62e-02	5.92e-02
398.7	1.31e-02	3.59e-02	5.87e-02
412.7	1.29e-02	3.56e-02	5.82e-02
426.8	1.28e-02	3.52e-02	5.77e-02
440.8	1.26e-02	3.49e-02	5.72e-02
454.8	1.25e-02	3.46e-02	5.67e-02
468.9	1.24e-02	3.43e-02	5.62e-02
482.9	1.22e-02	3.40e-02	5.57e-02

Vapour Thermal Conductivity: (W/mK) (Section 5.7.7)

MW: (g/mol)	400 K	700 K	1000 K
258.4	7.86e-06	2.15e-05	3.99e-05
272.5	7.62e-06	2.09e-05	3.88e-05
286.5	7.41e-06	2.03e-05	3.77e-05
300.5	7.21e-06	1.98e-05	3.67e-05
314.6	7.03e-06	1.93e-05	3.58e-05
328.6	6.86e-06	1.89e-05	3.50e-05
342.6	6.70e-06	1.84e-05	3.42e-05
356.6	6.55e-06	1.80e-05	3.34e-05
370.7	6.41e-06	1.76e-05	3.27e-05
384.7	6.28e-06	1.73e-05	3.21e-05
398.7	6.16e-06	1.69e-05	3.15e-05
412.7	6.04e-06	1.66e-05	3.09e-05
426.8	5.93e-06	1.63e-05	3.03e-05
440.8	5.82e-06	1.60e-05	2.98e-05
454.8	5.72e-06	1.58e-05	2.93e-05
468.9	5.62e-06	1.55e-05	2.88e-05
482.9	5.53e-06	1.53e-05	2.83e-05

Vapour Diffusion: (m^2/s) (Section 5.7.6)

a_C:	672.8
b_C:	0.444
a_B:	505.4
b_B:	0.478

Boiling and Critical Point Coefficients (Sections: 5.7.1 & 5.7.2) (Equations: 5.8 & 5.11)

a_V:	-6.17e-02
b_V:	3.98e-03
a_P:	21.8
b_P:	-3.35e-02

Critical Volume and Pressure Coefficients (Section: 5.7.1) (Equations: 5.9)

a_L:	4.36e+07
b_L:	1.59e+05

Enthalpy of Vaporization Coefficients (Section: 5.7.3) (Equations: 5.13)

a_L:	1.68e+00
b_L:	-2.91e-04
b_L:	6.48e-06

Liquid Specific Heat Coefficients (Section: 5.7.4) (Equation: 5.19)

a_1:	1.89e+00	b_1:	-7.79e-03
a_2:	-1.91e-02	b_2:	8.15e-04
a_3:	1.14e-05	b_3:	-4.66e-07
a_4:	-2.46e-09	b_4:	1.02e-10

Vapour Specific Heat Coefficients (Section: 5.7.5) (Equations: 5.25, 5.26 & 5.27)

a_D:	2.04e-09
b_D:	-2.00e-12
b_Φ:	240.0

Diffusion Coefficients (Section: 5.7.6) (Equation: 5.37)

a_D:	-1.80e-02
b_D:	1.16e-03
α_P:	1.00e-03

Liquid Specific Volume Coefficients (Section: 5.7.8) (Equation: 5.48)

a_{KC}:	-2.06e-02
b_{KT}:	9.38e-05
b_{KC}:	7.99e-06
b_{KT}:	-4.43e-08

Thermal Conductivity Coefficients (Section: 5.7.7) (Equation: 5.45, 5.46 & 5.47)

B Raw Py-FIMS Data

The following table contains the raw Py-FIMS data (Monreal and Jandl, 2012) from the fuel analysis (Explained in section 3.3.1). The total ion count (TII) is a measurement of the response for the particular species (Average of 3 trials). The mass charge ratio (m/z) is the mass of the ion divided by its charge (assume to be +1), this is roughly equal to the mol fraction. The names of the remaining categories are shown below.

TII	Total Ion Intensity (Total Ion Counts)
CHYDR	Carbohydrates
PHLM	Phenols + Lignin Monomers
LDIM	Lignin Dimers
LIPID	Lipids
ALKY	Alkyl Aromatics
NCOMP	Heterocyclic Nitrogen Containing Compounds
STEROL	Sterols
PEPTI	Peptides
SUBER	Suberin
FATTY	Free Fatty Acids
ISOM+1	13C Signals and M+1 Peaks

Legend: Py-FIMS Groups and Abbreviations

m\z (Da)	CHYDR	PHLM	LDIM	LIPID	ALKY	NCOMP	STEROL	PEPTI	SUBER	FATTY	m\z 15-56	ISOM+1	Unknown	(TII) Mean
16											x			0.00E+00
17											x			0.00E+00
18											x			0.00E+00
19											x			7.00E-04
20											x			0.00E+00
21											x			0.00E+00
22											x			0.00E+00
23											x			0.00E+00
24											x			0.00E+00
25											x			0.00E+00

26										x			0.00E+00
27										x			0.00E+00
28										x			7.00E-04
29										x			1.71E-02
30										x			0.00E+00
31										x			0.00E+00
32										x			0.00E+00
33										x			0.00E+00
34										x			0.00E+00
35										x			0.00E+00
36										x			0.00E+00
37										x			0.00E+00
38										x			0.00E+00
39										x			0.00E+00
40										x			0.00E+00
41										x			0.00E+00
42										x			1.10E-03
43										x			3.00E-01
44										x			5.30E-03
45										x			5.00E-04
46										x			0.00E+00
47										x			0.00E+00
48										x			0.00E+00
49										x			0.00E+00
50										x			0.00E+00
51										x			0.00E+00
52										x			0.00E+00
53										x			0.00E+00

54											x			2.00E-04
55											x			0.00E+00
56											x			1.11E-02
57								x						1.88E-02
58												x		4.00E-04
59							x							0.00E+00
60	x													1.60E-03
61												x		0.00E+00
62													x	0.00E+00
63													x	2.50E-03
64													x	0.00E+00
65													x	0.00E+00
66													x	0.00E+00
67							x							0.00E+00
68													x	4.00E-04
69													x	1.30E-03
70								x						5.80E-03
71												x		1.06E-02
72	x													2.00E-04
73								x				x		4.00E-04
74								x						0.00E+00
75								x						0.00E+00
76												x		0.00E+00
77													x	6.00E-04
78													x	0.00E+00
79							x							0.00E+00
80												x		0.00E+00
81							x							7.00E-04

82	x												0.00E+00
83												x	7.00E-04
84	x						x						5.40E-03
85											x		1.19E-02
86												x	0.00E+00
87							x						0.00E+00
88											x		0.00E+00
89												x	0.00E+00
90												x	0.00E+00
91							x						0.00E+00
92												x	0.00E+00
93												x	0.00E+00
94		x											0.00E+00
95						x							2.00E-04
96	x												0.00E+00
97							x				x		1.00E-03
98												x	2.00E-03
99							x				x		1.70E-03
100												x	0.00E+00
101												x	1.20E-03
102												x	0.00E+00
103						x							0.00E+00
104											x		9.00E-04
105												x	0.00E+00
106												x	7.00E-04
107												x	0.00E+00
108		x											0.00E+00
109						x							0.00E+00

110	x	x											7.00E-04
111						x							4.00E-04
112	x												5.00E-04
113											x		1.00E-03
114	x												0.00E+00
115							x						0.00E+00
116											x		1.00E-04
117												x	5.00E-04
118												x	1.20E-03
119												x	0.00E+00
120							x						2.30E-03
121											x		0.00E+00
122		x											0.00E+00
123						x							0.00E+00
124		x											0.00E+00
125						x							0.00E+00
126	x												1.90E-03
127											x		0.00E+00
128												x	0.00E+00
129							x						1.10E-03
130											x		7.00E-04
131												x	0.00E+00
132	x												4.00E-04
133											x		0.00E+00
134												x	6.60E-03
135							x				x		3.00E-03
136											x		1.00E-03
137						x							5.00E-04

138		x												0.00E+00
139						x								0.00E+00
140		x												9.00E-04
141												x		0.00E+00
142													x	1.60E-03
143												x		0.00E+00
144	x													5.00E-04
145												x		0.00E+00
146													x	0.00E+00
147													x	8.00E-04
148													x	9.10E-03
149												x		1.00E-03
150		x												0.00E+00
151												x		9.00E-04
152		x												0.00E+00
153						x								0.00E+00
154		x												7.00E-04
155												x		9.00E-04
156													x	0.00E+00
157												x		0.00E+00
158													x	2.10E-03
159													x	0.00E+00
160													x	3.80E-03
161						x								0.00E+00
162	x													8.00E-03
163												x		5.90E-03
164		x												0.00E+00
165												x		1.30E-03

166		x												9.00E-04
167						x								8.00E-04
168		x												0.00E+00
169												x		2.40E-03
170					x									0.00E+00
171												x		0.00E+00
172													x	0.00E+00
173													x	0.00E+00
174													x	3.40E-03
175													x	5.00E-04
176					x									7.60E-03
177												x		3.10E-03
178		x												5.00E-04
179												x		2.70E-03
180		x												1.00E-03
181						x								1.90E-03
182		x												0.00E+00
183						x								7.00E-04
184					x									4.30E-03
185												x		1.10E-03
186													x	1.20E-03
187													x	0.00E+00
188													x	5.70E-03
189													x	1.40E-03
190					x									1.67E-02
191												x		7.90E-03
192					x									2.00E-03
193												x		1.40E-03

194		x												1.60E-03
195						x								7.00E-04
196		x												9.30E-03
197												x		4.00E-03
198					x									8.80E-03
199												x		3.50E-03
200													x	3.30E-03
201													x	0.00E+00
202				x										1.37E-02
203						x								2.40E-03
204					x									2.02E-02
205												x		3.10E-03
206					x									6.70E-03
207												x		7.80E-03
208		x												7.90E-03
209												x		3.00E-03
210		x												4.08E-02
211												x		5.90E-03
212		x												2.62E-02
213												x		0.00E+00
214													x	7.60E-03
215													x	1.00E-03
216				x										2.35E-02
217												x		2.30E-03
218					x									3.85E-02
219												x		7.80E-03
220					x									5.10E-03
221												x		0.00E+00

222													x	2.28E-02
223													x	1.00E-03
224													x	7.24E-02
225													x	1.34E-02
226													x	5.05E-02
227													x	3.50E-03
228													x	1.53E-02
229													x	6.00E-04
230				x										6.20E-02
231												x		5.00E-03
232					x									1.17E-01
233						x								2.13E-02
234					x									2.08E-02
235												x		2.70E-03
236													x	9.98E-02
237													x	2.09E-02
238				x										2.51E-01
239													x	5.14E-02
240				x										1.83E-01
241													x	2.50E-02
242													x	2.50E-02
243													x	2.50E-03
244				x										5.27E-02
245						x								9.20E-03
246			x		x									1.37E-01
247												x		2.10E-02
248													x	1.67E-02
249													x	3.50E-03

250													x	1.08E-01
251													x	1.56E-02
252				x										2.98E-01
253													x	5.87E-02
254				x										2.61E-01
255						x								4.40E-02
256				x						x				4.09E-02
257						x								1.80E-03
258				x										6.75E-02
259												x		1.37E-02
260			x		x									1.66E-01
261												x		2.34E-02
262													x	3.34E-02
263													x	6.60E-03
264				x										1.51E-01
265													x	2.53E-02
266				x										4.85E-01
267													x	1.27E-01
268				x										5.23E-01
269													x	1.09E-01
270			x	x						x				5.35E-02
271						x								8.80E-03
272			x	x										1.25E-01
273												x		2.60E-02
274			x		x									2.92E-01
275												x		3.94E-02
276													x	5.49E-02
277													x	8.40E-03

278													x	1.81E-01
279													x	4.10E-02
280				x										7.59E-01
281													x	2.54E-01
282				x										7.06E-01
283													x	1.62E-01
284			x	x						x				9.07E-02
285						x								1.35E-02
286			x	x										1.44E-01
287												x		3.11E-02
288					x									2.79E-01
289												x		5.82E-02
290													x	8.81E-02
291													x	1.12E-02
292													x	2.32E-01
293													x	4.83E-02
294				x										9.27E-01
295													x	2.43E-01
296			x											8.43E-01
297												x		2.08E-01
298			x	x						x				1.04E-01
299												x		6.30E-03
300			x	x										1.43E-01
301												x		2.01E-02
302					x									3.03E-01
303												x		6.28E-02
304													x	9.37E-02
305													x	7.50E-03

306													x	2.83E-01
307													x	6.58E-02
308				x										1.22E+00
309													x	3.31E-01
310			x											8.26E-01
311												x		1.94E-01
312			x	x						x				1.11E-01
313												x		1.19E-02
314			x	x										1.69E-01
315												x		1.98E-02
316			x		x									2.74E-01
317												x		5.14E-02
318													x	1.04E-01
319													x	1.08E-02
320													x	3.11E-01
321													x	6.39E-02
322				x										1.31E+00
323													x	3.91E-01
324				x										9.16E-01
325													x	2.11E-01
326			x	x						x				9.92E-02
327												x		1.03E-02
328			x	x										1.28E-01
329												x		3.24E-02
330			x		x									3.08E-01
331												x		5.55E-02
332													x	1.01E-01
333						x								1.50E-02

334												x		3.02E-01
335													x	5.66E-02
336				x										1.01E+00
337													x	2.95E-01
338				x										6.05E-01
339													x	1.54E-01
340			x	x						x				1.27E-01
341												x		3.50E-02
342			x	x										2.05E-01
343												x		3.05E-02
344					x									2.37E-01
345													x	4.80E-02
346													x	1.04E-01
347													x	2.29E-02
348													x	2.56E-01
349													x	4.23E-02
350				x										7.20E-01
351													x	2.19E-01
352				x										9.47E-01
353													x	2.57E-01
354				x						x				1.15E-01
355												x		2.88E-02
356			x											1.47E-01
357												x		1.50E-02
358					x									1.88E-01
359						x								4.55E-02
360												x		1.15E-01
361													x	1.37E-02

362												x	2.02E-01
363						x							5.46E-02
364											x		5.69E-01
365												x	1.87E-01
366				x									1.09E+00
367												x	3.12E-01
368				x						x			1.23E+00
369											x		3.67E-01
370							x						3.37E+00
371												x	9.91E-01
372					x		x						5.43E-01
373											x		1.21E-01
374												x	8.45E-02
375												x	2.07E-02
376												x	2.10E-01
377												x	5.32E-02
378												x	7.09E-01
379												x	2.70E-01
380				x									2.38E+00
381											x		7.29E-01
382				x						x			1.76E+00
383											x		5.52E-01
384							x						5.50E+00
385												x	1.70E+00
386					x		x						9.75E-01
387											x		2.18E-01
388							x						1.28E-01
389											x		1.30E-02

390							x							2.15E-01
391												x		7.88E-02
392							x							8.58E-01
393						x								3.67E-01
394				x			x							2.03E+00
395												x		7.33E-01
396				x			x			x				5.68E+00
397												x		1.86E+00
398							x							1.44E+01
399												x		4.57E+00
400							x							2.14E+00
401												x		5.35E-01
402							x							1.91E-01
403												x		3.88E-02
404													x	3.15E-01
405													x	1.11E-01
406													x	8.07E-01
407													x	2.98E-01
408				x										1.44E+00
409												x		4.82E-01
410							x							1.10E+00
411												x		3.86E-01
412							x							7.68E-01
413												x		3.03E-01
414							x							6.53E-01
415												x		1.79E-01
416							x							1.35E-01
417												x		3.20E-02

418												x	1.62E-01
419												x	6.31E-02
420												x	6.58E-01
421												x	2.17E-01
422				x									6.15E-01
423											x		1.92E-01
424				x					x				2.34E-01
425											x		1.08E-01
426							x						2.34E-01
427											x		7.43E-02
428												x	3.76E-01
429												x	1.53E-01
430							x						1.99E-01
431											x		3.54E-02
432								x					2.07E-01
433											x		6.82E-02
434				x									7.54E-01
435												x	2.79E-01
436				x									3.28E-01
437												x	9.83E-02
438				x					x				6.40E-02
439											x		3.89E-02
440												x	6.67E-02
441												x	3.69E-02
442												x	1.14E-01
443												x	3.74E-02
444												x	5.47E-02
445												x	3.09E-02

446									x				9.88E-02
447												x	5.26E-02
448				x									4.11E-01
449													x	1.62E-01
450				x									2.12E-01
451													x	3.90E-02
452				x						x			3.08E-02
453												x	2.20E-03
454													x	6.35E-02
455													x	2.60E-02
456													x	8.11E-02
457													x	2.10E-02
458													x	8.22E-02
459													x	4.22E-02
460									x					3.99E-01
461												x		1.20E-01
462													x	2.72E-01
463													x	9.01E-02
464				x										1.16E-01
465													x	3.03E-02
466				x						x				1.12E-02
467												x		4.60E-03
468													x	2.71E-02
469													x	9.60E-03
470													x	6.16E-02
471													x	1.08E-02
472													x	4.25E-02
473													x	2.47E-02

474									x				9.33E-02
475												x	2.74E-02
476													x	2.18E-01
477													x	6.92E-02
478				x										8.47E-02
479													x	1.91E-02
480				x						x				1.46E-02
481												x		1.67E-02
482													x	1.93E-02
483													x	8.30E-03
484													x	2.64E-02
485													x	1.68E-02
486													x	1.04E-01
487													x	5.53E-02
488									x					1.05E-01
489												x		2.77E-02
490													x	1.05E-01
491													x	4.20E-02
492				x										3.40E-02
493													x	4.30E-03
494				x						x				4.50E-03
495												x		0.00E+00
496													x	1.54E-02
497													x	9.20E-03
498													x	3.50E-03
499													x	5.50E-03
500													x	1.10E-02

TOTAL													99.46